

Thermal structure of the southern Caribbean and NW South America: implications for seismogenesis

Ángela María Gómez-García^{1,2,+}, Álvaro González^{1,3}, Mauro Cacace¹, Magdalena Scheck-Wendroth¹, Gaspar Monsalve⁴

¹ GFZ German Research Centre for Geosciences, Telegrafenberg, 14473, Potsdam, Germany.

² Corporation Center of Excellence in Marine Sciences (CEMarin). Bogotá, Colombia.

³ Centre de Recerca Matemàtica (CRM). Campus UAB, Edifici C. 08193, Bellaterra (Barcelona), Spain.

⁴ Universidad Nacional de Colombia, Facultad de Minas, Medellín, Colombia.

Corresponding author: Ángela María Gómez-García (angela@gfz-potsdam.de), ⁺Now at Geosciences Barcelona (GEO3BCN), CSIC, Lluís Solé i Sabarís s/n. 08028, Barcelona, Spain

Abstract. The seismogenesis of rocks is mainly affected by their mineral composition and in-situ conditions (temperature and state of stress). Diverse laboratory experiments have explored the frictional behavior of the rocks and rock-forming minerals most common in the crust and uppermost mantle. However, it is debated how to "up-scale" these results to the lithosphere. In particular, most earthquakes in the crust occur down to the crustal seismogenic depth (CSD), which is a proxy to the brittle-ductile transition. The CSD largely limits the depth down to which crustal earthquakes may rupture, and therefore influences the seismic hazard of any region. In this study we propose a workflow to up-scale and validate those laboratory experiments to natural geological conditions relevant for crustal and upper mantle rocks. We used the southern Caribbean and NW South America as a case study to explore the three-dimensional spatial variation of the CSD and the temperatures at which crustal earthquakes likely occur. A 3D steady-state thermal field was computed for the region, using a finite element scheme using the software GOLEM, considering the uppermost 75 km of a previously published 3D data-integrative lithospheric configuration, lithology-constrained thermal parameters, and appropriate upper and lower boundary conditions. The model was validated using additional, independent measurements of downhole temperatures and heat flow. We found that the majority of crustal earthquakes nucleate at temperatures less than 350°C, in agreement with frictional experiments of typical crustal rocks. A few outliers with larger hypocentral temperatures evidence nucleation conditions consistent with the seismogenic window of olivine-rich rocks, and can be due either to uncertainties in the Moho depths and/or in the earthquake hypocenters, or to the presence of ultramafic rocks within different crustal blocks and allochthonous terranes accreted to this complex margin. Moreover, the spatial distribution of crustal seismicity in the region correlates with the geothermal gradient, with no crustal earthquakes occurring in domains with low thermal gradient. Finally, we find that the largest earthquake recorded in the region ($M_w=7.1$, Murindó sequence, in 1992) nucleated close to the CSD, highlighting the importance of considering this lower stability transition for seismogenesis when characterizing the depth of seismogenic sources in hazard assessments. The approach presented in this study goes beyond a statistical approach in that the local heterogeneity of physical properties is considered in our simulations and additionally validated by the observed depth distribution of earthquakes. The coherence of the calculated hypocentral temperatures with those expected from laboratory measurements provides additional support to the model. This approach can be applied to other tectonic settings worldwide, and it could be further refined as new, high-quality hypocentral locations and heat flow and temperature observations become available.

Definición de estilo

Eliminado: Crustal Seismogenic Thickness and

Eliminado: S

Eliminado: (angela@gfz-potsdam.de).

Eliminado: crustal seismogenic thickness (CST) has direct impl

Eliminado:) and by the rocks' heterogeneous composition.

Eliminado: materials forming

Con formato

Eliminado: remains a matter of debate

Con formato

Eliminado: scale of the

Con formato

Eliminado: the conclusions derived from these studies.

Con formato

Eliminado: these

Eliminado: of

Eliminado: T...and the

Eliminado: The...3D steady-state thermal field was computed f

Eliminado: taking into account...the uppermost 75 km of a prev

Eliminado: .

Con formato

Eliminado: events...nucleate at temperatures of

Con formato

Eliminado: general ...greement with frictional experiments of t

Eliminado: in the...hypocentral temperatures evidenceshowcase

Con formato

Eliminado: linked

Con formato

Eliminado: the...allochthonous crustal

Eliminado: Our results suggest...that the two ...argest earthqua

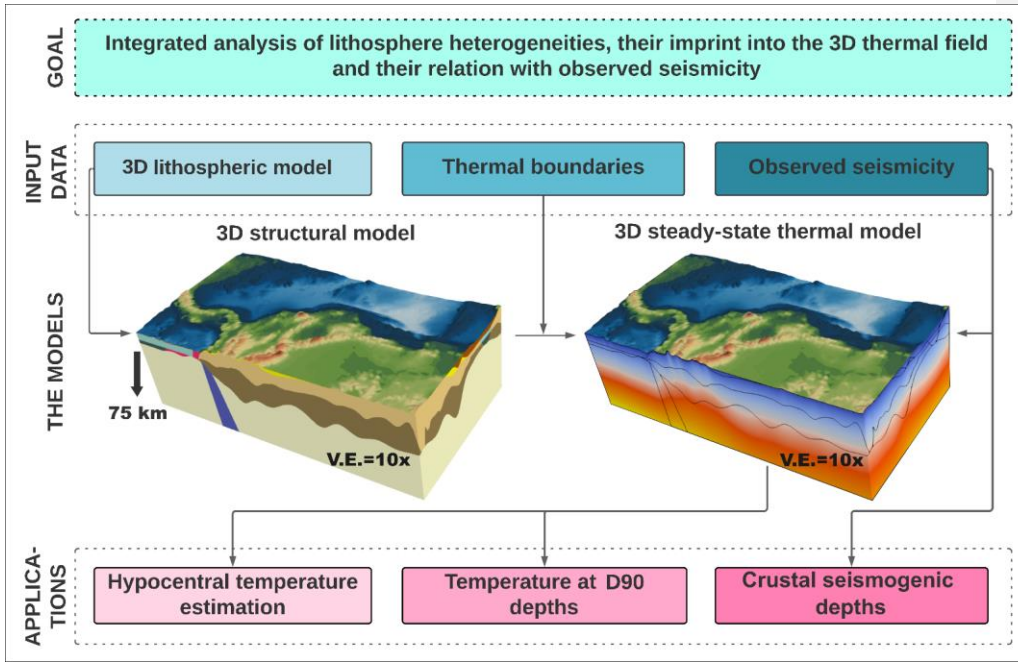
Eliminado: $M_s=6.8$ and $M_s...7.13...$ Murindó sequence, in 1992

Con formato

Eliminado: assessment studies.

Con formato

Con formato



Introduction

The spatial distribution of seismicity is controlled by the mechanical properties of the hosting rocks, and therefore by factors such as mineral composition and grain size, as well as by the in-situ temperature, pressure and strain rate conditions (e.g.: Chen et al., 2013; Zielke et al., 2020). Laboratory experiments indicate a range of limiting temperatures for seismogenesis, i.e.: temperatures at which rocks and mineral assemblies exhibit stick-slip behavior.

Granitic rocks exhibit seismic behavior at temperatures between 90-350°C, gabbro between 200-600°C, and olivine gouge between 600-1000°C (King and Marone, 2012; Scholz, 2019). These ranges, however, are only a proxy to natural conditions, where rocks are more heterogeneous than the laboratory samples and may have a more complex behavior. For example, mixtures of 65% illite and 35% quartz might exhibit a seismogenic window between 250 and 400°C, while replacing the illite with muscovite implies a new window between 350 and 500°C (Scholz, 2019).

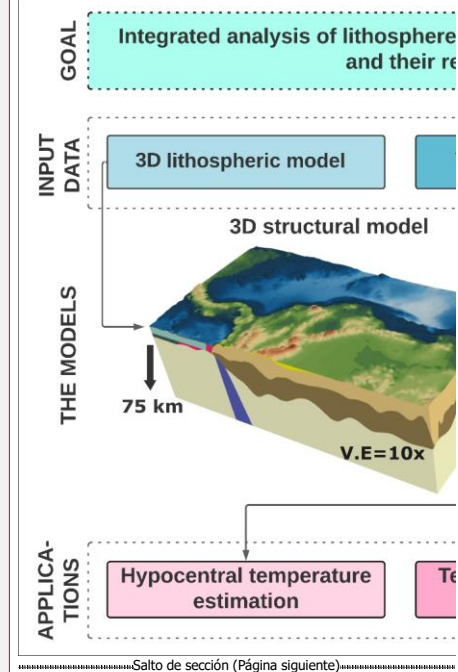
The upper temperature threshold for seismogenesis in mantle-forming minerals is highly debated. Some authors defined a rather strict limit 600°C (e.g.: Craig et al., 2012; McKenzie et al., 2005), but new evidence suggests higher values. For example, Ueda et al. (2020) found that the brittle-to-ductile transition in peridotite occurs at ~720 °C. Similarly, Grose and Afonso (2013) studied the evolution of the oceanic lithosphere using more realistic thermal models than those assumed by McKenzie et al. (2005), and found a brittle-ductile transition closer to the 700-800°C isotherms, depending on the estimated mantle temperature. So, apart from subduction zones, it is generally considered that earthquakes nucleate within the crust at $T < 350 \pm 50^\circ\text{C}$, and at $T < 700 \pm 100^\circ\text{C}$ in the mantle (see review by Chen et al., 2013).

As a result of these physical constrains, seismicity is typically distributed within the crust down to a maximum depth (Marone and Scholz, 1988; Marone and Saffer, 2015; Wu et al., 2017; Scholz, 2019). Such a lower limit, the crustal seismogenic depth (CSD) is usually quantified as the depth above which a large percentage (such as 90% or 95%) of the crustal hypocenters have been recorded (Omuralieva et al., 2012; Sibson, 1982; Tanaka, 2004; Wu et al., 2017). This estimate has also been discussed to provide a conservative, minimum bound to the depth to the brittle-ductile transition (Zuza and Cao, 2020). In converging margins, such percentiles may be calculated from crustal seismicity alone, in order to avoid mixing different statistical earthquake depth distributions arising from the subduction interface or the underlying slab with that of the upper plate (Tanaka, 2004; Wu et al., 2017).

In an attempt to up-scale the results of laboratory experiments, previous studies tried to model the thermal field of active systems and to target the temperature ranges at which earthquakes likely nucleate (Gutscher et al., 2016; Oleskevich et al., 1999; Zuza and Cao, 2020). The results from these efforts indicate that in intracontinental faults, the brittle-ductile transition seems to be controlled by variations in the geothermal gradient, being limited by the 300-350°C isotherm, consistent with a quartz-dominated lithology (Zuza and Cao, 2020). Other works (Omuralieva et al., 2012; Tanaka, 2004), support that high heat flow correlates with a shallow CSD, especially for regions with high geothermal gradient (e.g.: $> 100^\circ\text{C}/\text{km}$). However, in regions where the geothermal gradient is not particularly high, the relationship between the CSD and the thermal state of the crust is not clear (see Fig. 1 in Tanaka, 2004). As a major limitation, most of these approaches consider a simplified lithospheric structure, disregarding in particular tectonic assemblies that can considerably affect the three-dimensional configuration of the thermal field, such as the heterogeneous geometries and properties of the lithospheric layers and the thermal blanketing effect of the sediments (e.g.: Cacace and Scheck-Wenderoth, 2016).

Eliminado: became eventually available for testing and validating the thermal models.

.....Salto de sección (Página siguiente).....



155 This paper focuses on the thermal structure of southern Caribbean and NW South America (Fig. 1a) and its implication for seismogenesis, using a 3D data-integrative numerical modelling approach, and relying on an earthquake catalogue which selects the best-located earthquakes reported in global databases since 1980. We develop a thermal model for the lithosphere down to 75 km depth, to calculate the temperatures at which crustal earthquakes likely nucleate. Also, we systematically map the spatially variable CST, and its temperature according to the model. We do not attempt to account for transient effects in the seismogenic zone configuration, but rather focus on its regional variations as averaged over time.

160 The complex tectonic setting of the study area poses a challenge to model a realistic thermal field that allows upscaling the seismogenesis from laboratory experiments. This includes the convergence of at least four tectonic plates, several tectonic blocks, the accretion of allochthonous terranes, and the presence of continental basins with sediment thicknesses up to 8 km (Mora-Bohórquez et al., 2020) (Fig. 1b).

165 As the extent of the CST is influenced by factors that vary in space, such as lithology and local geothermal gradients (Hirth and Beeler, 2015; Zielke et al., 2020), we computed the 3D steady-state thermal response using a recently published 3D structural and density model of the study area, which is consistent with different geological and geophysical observations, including gravity (Gómez-García et al., 2020, 2021). A steady-state approach can be regarded as appropriate for this analysis since: 1) we preferentially target crustal earthquakes, 2) The subducting segments of the Nazca and Caribbean slabs in the study area are flat (Gómez-García et al., 2021; Kellogg et al., 2019; Sun et al., 2022), implying that the subducting velocities might be lower than in steep slab segments (Currie and Copeland, 2022; Schellart and Strak, 2021). So, the transient effects of dynamic changes and mantle wedge cooling due to subduction occur in much longer temporal scales than those of the heat transport in the upper lithosphere and of the earthquake cycle. And 3) we are already considering the mantle imprint on the temperature field at 75 km depth as a lower boundary condition.

170 The main advantage of our approach is to provide a comprehensive view of the system's heterogeneities, their contribution to the thermal field, and the long-term geological timescale given by the mantle thermal contribution and the 3D present-day lithospheric configuration.

175 Few earthquakes with magnitude $M > 7.0$ have been recorded in northern South America since the deployment of modern seismological networks, but there are historical records of earlier ones, for example, the shock which destroyed the city of Santa Marta, Colombia, in 1834. Similarly, paleoseismological studies in western Venezuela identified the fault rupture of other events with estimated magnitudes $M > 7.0$ (e.g.: Audemard, 1996; Pousse-Beltran et al., 2018). Overall, there is a substantial seismic hazard in the region (Pagani et al., 2018; Arcila et al., 2020), with highly populated centers located close to shallow active faults, which can generate devastating earthquakes (Veloza et al., 2012). A better understanding of the regional seismogenesis can significantly contribute to improve future seismic hazard and risk assessments.

2 Study area

180 The study area (5° - 15° N and 63° - 82° W, Fig. 1a) encompasses a domain where the Caribbean and Nazca (Coiba) flat slabs interact at depth (Gómez-García et al., 2021; Kellogg et al., 2019; Sun et al., 2022). This interaction resulted in a complex tectonic setting at the scale of the whole lithosphere, and in large uncertainties in the estimated depths of the Moho interface (Avellaneda-Jiménez et al., 2022; Poveda et al., 2015; Reguzzoni and Sampietro, 2015). The present-day flat slab geometry has been established since about 6 Ma, when the Nazca tear developed separating the north (flat) and south (step) segments (Wagner et al., 2017). As a result, the volcanic activity has ceased in the continental crust of the overriding plate of the north

Eliminado: The crustal seismogenic thickness (CST) encloses the portion of the crust where the majority of earthquakes occur. Its upper boundary, hereafter referred to as the upper stability transition (UST), demarks the onset depth of seismicity. Its lower boundary, referred to as the lower stability transition (LST), defines the cutoff depth of seismicity (Marone & Saffer, 2015; Marone & Scholz, 1988; Scholz, 2019; Wu et al., 2017). The LST can also be used as a conservative upper estimate of the brittle-ductile transition (BDT) (e.g.: Zuzza & Cao, 2020). The depths of both the UST and the LST are usually determined based on imposed percentiles of the statistical distribution of earthquake hypocentral depths (e.g.: Marone & Scholz, 1988; Sibson, 1982; Wu et al., 2017). The seismogenic crust is then defined as the portion of the crust that contains a prescribed (i.e., statistically significant) percentage of the recorded earthquakes. ¶ The spatial distribution of seismicity is controlled by the mechanical properties of the hosting crustal rocks, and therefore by factors such as composition, grain size and mineral assemblage, as well as by the in-situ temperature, pressure and strain rates conditions (e.g. Chen et al., 2013; Zielke et al., 2020). Laboratory experiments are indicative of a range of limiting temperatures for seismogenesis, i.e.: temperatures at which rocks and mineral assemblages exhibit stick-slip behavior. For example, granitic rocks exhibit seismic behavior at temperatures between 90-350°C, gabbro between 200 and 600°C, and olivine gouge between 600 and 1000°C (Scholz, 2019, and references therein). Apart from subduction zones, it is generally considered that earthquakes nucleate within the crust at $< 350 \pm 50^{\circ}$ C, and at $< 700 \pm 100^{\circ}$ C in the mantle (see review by Chen et al., 2013). ¶ As an attempt to up-scale the results of laboratory experiments, previous studies have aimed at modelling the thermal field of active systems targeting the temperature ranges at which earthquakes can nucleate (e.g.: Gutscher et al., 2016; Oleskevich et al., 1999; Zuzza & Cao, 2020). The results from these efforts suggest that in faults located within the continents, the BDT seems to be controlled by variations in the geothermal gradient, being limited by the 300-350°C isotherm, consistent with a quartz-dominated lithology (e.g.: Zuzza & Cao, 2020). Nevertheless, most of these approaches usually consider a simplified lithospheric structure, disregarding particular tectonic assemblages that can considerably affect the three-dimensional configuration of the thermal field (e.g. Cacace and Scheck-Wenderoth, 2016). Moreover, the majority of studies have targeted preferentially regions away from active subduction zones (Chen et al., 2013). ¶ In this paper, we systematically map the CST and the temperatures at which crustal earthquakes nucleate in the South Caribbean and NW South America (Fig. 1). The complex tectonic setting poses a challenge to compare the results from laboratory experiments, including the convergence of at least four tectonic plates, the accretion of several allochthonous terranes, and the presence of continental sedimentary basins with thicknesses of up to 8 km (Mora-Bohórquez et al., 2020). Although few events with magnitude $M > 7.0$ have been recorded in northern South America since the deployment of modern seismological networks, there are historical records of earlier great earthquakes, for example, the shock which destroyed the city of Santa Marta, Colombia, in 1834. Similarly, ...

segment, which spatially corresponds to our study area. This allows us to consider that the propagation of heat within the crust is mainly driven by conduction (e.g.: Liu et al., 2021).

Figure 1a depicts the selected crustal earthquakes in the region (details in Sect. 3.2.1) and active fault traces. For the sake of clarity, in the remaining of the study we will focus on three specific sub-regions, marked by blue boxes in Fig. 1a. Our choice stems from the fact that these regions have contrasting tectonic environments, a heterogeneous spatial distribution of crustal seismicity and diverse allochthonous terranes accreted to the NW margin of South America (Fig. 1b). Such terranes resulted from the migration of the Caribbean Large Igneous Plateau (C-LIP) from the Pacific towards the present-day Caribbean plate location. The collision of the C-LIP with the continental margin of South America defined not only a broad sheared margin, but also extended fragments of mafic and ultramafic rocks associated to mantle-plume processes, and emplaced oceanic crust and remnants of island arcs (see Boschman et al., 2014; Kennan and Pindell, 2009; Montes et al., 2019). As a consequence, large-scale sutures (faults) act as major boundaries between these terranes (Kennan and Pindell, 2009).

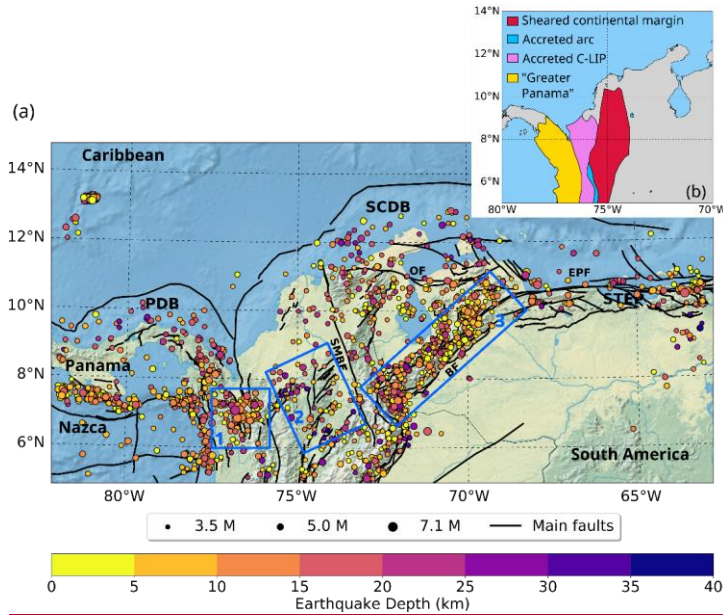


Figure 1. (a) Crustal earthquakes and active faults in the study area. Only the earthquakes with the best determined hypocentral depths in the region are represented (Sect. 3.2.1). Blue boxes: Sub-regions discussed in the main text. Black lines: Active fault

traces as compiled by (Styron et al., 2020; Veloza et al., 2012). PDB = Panama deformed belt, SCDB = South Caribbean Deformed Belt and STEP = Subduction-Transform-Edge-Propagator fault system. Main fault systems are: BF = Boconó Fault, SMBF = Santa Marta - Bucaramanga Fault, EPF = El Pilar Fault, and OF = Oca-Ancón Fault. (b) Simplified map of accreted terranes in NW South America (after Boschman et al., 2014; Kennan and Pindell, 2009).

335 Region 1 corresponds to the area around the Murindó seismic cluster (Dionicio and Sánchez, 2012). In this region, the Uramita fault system (UF, Fig. 3) acts as the suture between the (mainly) oceanic terranes of the western Cordillera, and the “Greater Panama” block (Fig. 1b), also called Panamá-Chocó block, dominated by plateau and magmatic arc terranes (Montes et al., 2019; Mosquera-Machado et al., 2009). Diverse active faults have been described in this area, including the Atrato, Mutatá and Murindó systems (MF, Fig. 3). The latter has been considered responsible for the $M_w = 6.6$ foreshock and $M_w = 7.1$ mainshock events, that occurred on 17th and 18th October 1992, respectively (Mosquera-Machado et al., 2009), the largest earthquakes recorded in the study region since the 1980s. The mainshock caused widespread liquefaction, landslides, complete destruction of the center of Murindó town and even building damages in Medellín, a city located more than 130 km away from the epicenter (Mosquera-Machado et al., 2009). In terms of recorded seismicity, this region is characterized by a dense occurrence of earthquakes at depths shallower than 25 km.

340 Region 2 includes the Otú, Palestina and El Espíritu Santo fault systems (Paris et al., 2000). The Palestina fault is a NE-SW strike-slip, right-lateral system that cuts the Central Cordillera, and its formation may have been associated to the oblique subduction of the oceanic lithosphere during the Late Cretaceous (Acosta et al., 2007). This system can be interpreted as the northward continuation of a large-scale brittle suture of different terranes (Kennan and Pindell, 2009). Hereafter, we will refer to the Palestina and Otú-Pericos faults altogether as the Otú-Palestina fault system (OPF, Fig. 3), even though those two structures might be genetically different (Restrepo and Toussaint, 1988). The right-lateral Espíritu Santo fault (ES, Fig. 3) can be considered as a part of the large-scale suture zone defined by the Romeral Fault System (RFS, Fig. 3, Noriega-Londoño et al., 2020). This region concentrates most of the deepest seismic events of the study area.

345 Region 3 comprises the Venezuelan Andes including the NE-SW Boconó fault system (BF, Fig. 1a). This active fault network accommodates most of the displacement of the Maracaibo block (delimited by the OF, BF and SMBF fault systems, Fig. 1) with a right-lateral strike-slip motion, and serves as its boundary with South America (Pousse-Beltran et al., 2018 and references therein). The seismicity is deeper in the SW portion of the fault system and shows a smooth transition where it shallows towards the NE.

350 **3 Methods**

3.1 Steady-state 3D thermal model and input data

360 The main mechanism of heat transport within the lithosphere is thermal conduction. Considering the short temporal scales of the seismic events compared to the scales at which the thermal field evolves in the crystalline crust, a first-order calculation can be obtained by a steady-state approach (Turcotte and Schubert, 2014), described by the following equation:

$$H = \nabla(\lambda_b \nabla T) \quad \text{Eq. (1)}$$

where H is the radiogenic heat production, ∇ is the nabla operator, and λ_b the bulk thermal conductivity. The steady-state 3D thermal field is here computed using a numerical model based on the finite-element method with the software GOLEM (see details in Cacace and Jacquey, 2017). We used the uppermost 75 km of an available 3D data-constrained structural and density model (Gómez-García et al., 2020, 2021) (Fig. 2a) as the main input, where dominant lithologies were assigned to individual layers. In the computed thermal field (Fig. 2b), the heat transport within the lithosphere depends on the temperatures used as boundary conditions (Fig. 2c and 2d) and on the thermal properties of each lithospheric layer (H and λ_b), the values of which have been assigned based on the main lithology as explained in more detail later in the text. The thermal model is published as a separate database (Gómez-García et al., 2023).

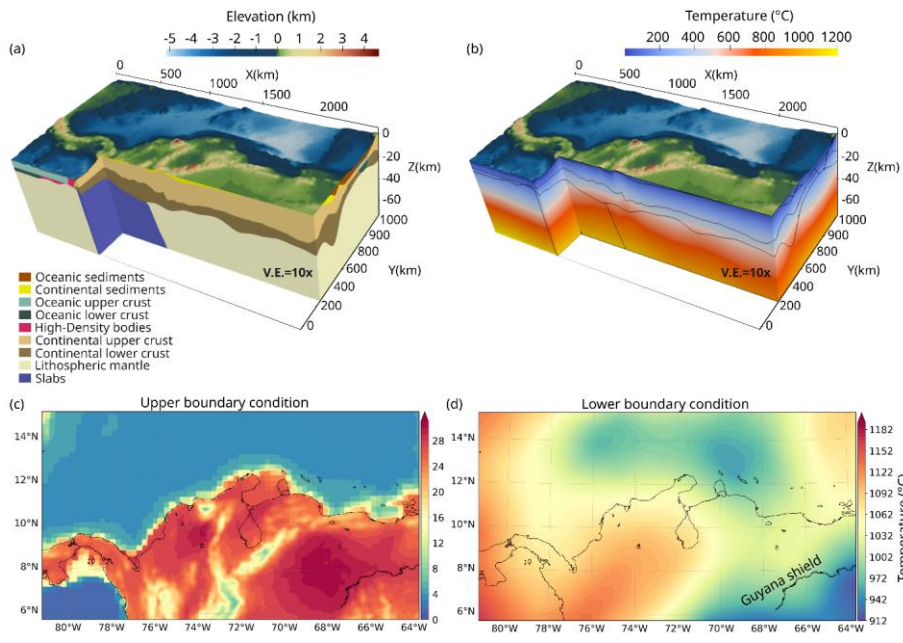


Figure 2. 3D thermal model with its structural layers and boundary conditions. The thermal calculation was based on a 3D data-integrative model of the study area, which includes the thermal signature of the heterogeneities from the lithospheric mantle (75 km depth) to the surface. (a) 3D structural model (Gómez-García et al., 2020, 2021) used to compute the 3D thermal field. The model includes fifteen different layers, although the figure only depicts those visible in the 3D view. Lithology-constrained thermal parameters were assigned to each of them (Table 1). (b) 3D steady-state thermal field, with the boundaries

between layers of the structural model depicted as black thin lines. Both the structural and thermal models are shown with a 10X vertical exaggeration. (c) Upper boundary condition, which integrates the temperatures over the continent from the ERA5-Land dataset (Copernicus Climate Change Service, 2019) with those on the seabed from the GLORYS dataset (Ferry et al., 2010). (d) Lower boundary condition, set as the temperatures at 75 km depth, after converting S-wave velocities into temperatures (details in Sect. 3.1.2).

3.1.1 Lithospheric structural model and definition of thermal properties

The data-integrative and gravity-constrained structural and density model of the South Caribbean margin (as detailed in Gómez-García et al., 2020, 2021) (Fig. 2a) represents the first-order geological complexity of the Caribbean realms by including fifteen different layers (Table 1). In order to achieve a detailed spatial resolution for the thermal calculations, the structural model has been refined to a 5 km x 5 km horizontal cell size.

The density of each layer (as constrained by Gómez-García et al. (2021)) helps inferring its main lithology, which in turn, allows defining its own values of thermal properties, namely the thermal conductivity and radiogenic heat production (e.g.: Ehlers, 2005; Hasterok et al., 2018; Vilà et al., 2010), as detailed in Text S1. Text S2 presents a sensitivity analysis in which we explored the response of 25 different models which considered a range of feasible variations in the thermal properties. The best model was selected (as discussed in Sect 4.1) as the one that independently best reproduced the temperatures measured in boreholes.

Table 1 lists the lithologies inferred for each layer, compatible with derived densities and with the geologic and tectonic setting of the southern Caribbean region and the northern Andes, the final thermal properties used for the modelling (best fitting model), and the rationale behind each choice.

3.1.2 Upper and lower boundary conditions

The thermal upper boundary condition (Fig. 2c) was defined as the temperature field on the solid Earth surface, obtained by integrating the average onshore surface temperatures from the ERA5-Land dataset, from January 2015 to April 2019 (Copernicus Climate Change Service, 2019), and the average temperatures at the seafloor from GLORYS reanalysis (Ferry et al., 2010) for the year 2015. In the modelled domain, the integrated temperature field ranges from $\sim 1^{\circ}\text{C}$ on the seafloor of the Pacific Ocean to a maximum of $\sim 30^{\circ}\text{C}$ over the Venezuelan territory. As expected, the temperatures over the mountains are the lowest within the continental realm, with an average of $\sim 8^{\circ}\text{C}$.

The lower boundary condition was defined as the temperature field at 75 km depth (Fig. 2d). It was calculated from a conversion of the S-wave velocities from the SL2013sv tomographic model (Schaeffer and Lebedev, 2013) to temperatures, following the approaches of Goes et al. (2000) and Meeßen (2017), and adopting the reference composition listed in Table S3. This thermal boundary depicts two cold domains: the Guyana shield, with minima $\sim 912^{\circ}\text{C}$, and within the Caribbean region, with a mean value of $\sim 972^{\circ}\text{C}$. In contrast, in the region of the Nazca and Caribbean flat slabs, the temperatures are higher than the surroundings, reaching up to $\sim 1100^{\circ}\text{C}$. All lateral borders of the model are assumed to be closed.

Eliminado: The study area (5° - 15°N and 63° - 82°W , Fig. 1) includes the interaction of the Caribbean and Nazca (Coiba) flat-slabs at depth (Gómez-García et al., 2021; Kellogg et al., 2019; Sun et al., 2022). Due to this interaction, a complex tectonic setting is present at lithospheric-scale, including large uncertainties in depths to the Moho interface (e.g.: Avellaneda-Jiménez et al., 2022; Poveda et al., 2015; Reguzzoni & Sampietro, 2015). ¶

Figure 1. depicts the crustal seismic catalogue derived from the ISC Bulletin (International Seismological Centre, 2022, see Sect. 3.2.1), and active fault traces. For the sake of clarity, in the remaining of the study we will focus on three specific sub-regions, marked by blue boxes in Fig. 1. Our choice stems from the fact that these regions have contrasting tectonic environments, a heterogeneous spatial distribution of crustal seismicity and diverse allochthonous terrane ...

Con formato: Alemán (Alemania)

Eliminado: derived

Eliminado: Muñoz Sabater

Eliminado:),

Eliminado: (Ferry et al., 2010)

Eliminado: in

Con formato: Alemán (Alemania)

Eliminado: of

Con formato: Alemán (Alemania)

Eliminado: for the period used in this research

Table 1. Thermal properties defined for each lithospheric layer and their densities after Gómez-García et al. (2020, 2021). λ_b : Bulk thermal conductivity. H : Radiogenic heat production. C-LIP: Caribbean Large Igneous Plateau. See details in Texts S1 and S2. Reference abbreviations: ^aTurcotte and Schubert (2014), ^bVilà et al. (2010), ^cNeill et al. (2011), ^dKerr (2014), ^eMontes et al. (2019).

Layer	Density (kg m ⁻³)	λ_b (W m ⁻¹ K ⁻¹)	H (μ W m ⁻³)	Rationale for λ_b	Reference for H
Oceanic sediments	2350	2.55	1.1	Average between sandstone, limestone and shale ^a	Mean value for sedimentary rocks ^b
Continental sediments	2500	3.5	1.19	Assuming sandstones ^a	Mean value for detritic sedimentary rocks ^b
Oceanic upper crust	3000	2.1	0.358	Mean value for basalts ^a	Mean value for basalts ^b
Low density bodies (Aves Ridge)	2900	2.6	1.07	Average for basalts and granites ^a following the composition by ^c	Eq. S1, using the average concentration of U, Th and K for Aves Ridge samples ^c
High density bodies in the upper oceanic crust	3250	2.93	0.057	Average for basalts, gabbros and peridotites ^a assuming a C-LIP mixed composition	Eq. S1, using the average concentration of U, Th and K for C-LIP samples ^d
Oceanic lower crust	3100	2.95	0.468	Mean value for gabbros ^a	Mean value for gabbros ^b
Low density bodies in the lower oceanic crust (Aves Ridge)	3000	2.6	1.07	Average for basalts and granites ^a following the composition by ^c	Eq. S1, using the average concentration of U, Th and K for Aves Ridge samples ^c
High density bodies in the lower oceanic crust	3250	2.93	0.057	Average for basalts, gabbros and peridotites ^a assuming a C-LIP mixed composition	Eq. S1, using the average concentration of U, Th and K for C-LIP samples ^d

Eliminado: The temperature field at 75 km depth was defined as the lower boundary condition (Fig 2d). It was calculated from a conversion of the S-wave velocities from the SL2013sv tomographic model (Schaeffer and Lebedev, 2013) to temperatures, following the approaches of Goes et al. (2000) and Meeßen (2017) and the composition shown in Table S3. This thermal boundary depicts two cold domains: the Guyana shield, with minimum temperatures of ~912°C, and within the Caribbean region, with a mean value of ~972°C. In contrast, the region where the Nazca and Caribbean flat slabs are present is hotter than the surroundings, reaching up to ~1100°C. All lateral borders of the model are assumed to be closed.

.....Salto de sección (Página siguiente).....
Table 1. Thermal properties defined for each lithospheric layer. Densities from Gómez-García et al. (2021). λ_b : Bulk thermal conductivity. H : Radiogenic heat production. C-LIP: Caribbean Large Igneous Plateau. See details in Text S1 and S2.†

Con formato: Sin control de líneas viudas ni huérfanas

Con formato: Fuente: 10 pto

Con formato: Sin control de líneas viudas ni huérfanas

Con formato: Sin control de líneas viudas ni huérfanas

Con formato: Sin control de líneas viudas ni huérfanas

Con formato: Sin control de líneas viudas ni huérfanas

Con formato: Sin control de líneas viudas ni huérfanas

Con formato: Sin control de líneas viudas ni huérfanas

Con formato: Sin control de líneas viudas ni huérfanas

Con formato: Sin control de líneas viudas ni huérfanas

Continental upper crust	2750	2.4	0.6	Assuming a granitic composition ^a	Assuming a granitic composition ^b
Low density bodies in the upper continental crust	2600 - 2650	2.1	0.4	Assuming a basaltic composition ^a	Assuming a basaltic composition ^b
High density body in the upper continental crust (Santa Marta massif)	3000	2.95	0.667	Mean value for gabbros ^a assuming a magmatic composition ^c	Assuming a gabbroic composition ^b
Continental lower crust	3070	2.4	0.5	Assuming a granitic composition ^a	Assuming a granitic composition ^b
High density subcrustal bodies	3242	4.15	0.01	Mean value for dunites ^a assuming a depleted, high-density mantle material	Value for depleted peridotites ^b
Slab	3163	3.3	0.001	Assuming a prevalence of peridotites ^a	Eq. S1, using the average concentration of U, Th and K reported for depleted mantle ^a
Lithospheric mantle	3D solution	3	0.012	Assuming a peridotitic composition ^a	Eq. S1, using the average concentration of U, Th and K reported for mantle ^a

Con formato: Sin control de líneas viudas ni huérfanas

Con formato: Sin control de líneas viudas ni huérfanas

Con formato: Sin control de líneas viudas ni huérfanas

Con formato: Sin control de líneas viudas ni huérfanas

Con formato: Sin control de líneas viudas ni huérfanas

Con formato: Sin control de líneas viudas ni huérfanas

Con formato: Sin control de líneas viudas ni huérfanas

3.1.3 Data available for validating the thermal model

We validated the 3D thermal model (Sect. 4.1) by comparing available measurements of downhole temperatures (ANH, 2020) and surface heat flow (Lucazeau, 2019) -not used as model inputs, against the corresponding modelled values. The locations of the control points are shown in Fig. 3. Our goal was to minimize the misfit between the observed and modelled values. We found the modelled temperatures at the downhole sites to be particularly sensitive to changes in the thermal properties, thus allowing tuning these (Text S2 and Fig. S1). Heat flow values are, by definition, less reliable than direct temperature measurements. Thus, we have used only the heat flow with the highest qualities (error range between 10% and 20%, Lucazeau, 2019) for a secondary check. In general, the measured heat flow is lower within the Caribbean Sea (40-80 mW m⁻²) than in the Pacific Ocean (>80 mW m⁻²). Minima (10-40 mW m⁻²) are found close to the area of influence of the Magdalena Fan depocenter (MFD, Fig. 3), likely as a result of the thermal blanketing by this thick sedimentary sequence (Scheck-Wenderoth and Maystrenko, 2013).

3.1.4 Geothermal gradient

We showcase the spatial variations in the geothermal gradient to demonstrate that 3D modelling is necessary to realistically calculate the thermal field in the study area. The geothermal gradient (∇T) was obtained, considering the modelled temperature (T_{ij}) at different depth levels (z_{ij}), following Eq. 2. As the geothermal gradient is not constant with depth, we mapped its variation for depths ranging from the solid Earth surface ($z=0$) down to $z=30$ km, with incremental steps of 3 km (Fig. S6). Additionally, we mapped the geothermal gradient from $z=0$ to $z=20$ km, the latter being approximately the average crustal seismogenic depth in the region (Sect. 4.3).

$$\nabla T(z) = \frac{T_i - T_j}{z_i - z_j} \quad \text{Eq. (2)}$$

A similar approach for calculating the geothermal gradient based on 3D thermal models was followed by Gholamrezaie et al. (2018), also using a 3D modelling scheme in which the geological heterogeneities of the system

Eliminado: ^aTurcotte & Schubert (2002). ^bVilà et al. (2010). ^cNeill et al. (2011). ^dKerr (2014). ^eMontes et al. (2019).

3.1.3 Validation of the modelled temperatures¶

The calculated 3D thermal field was validated by comparing measurements available from downhole temperatures (ANH, 2020) and surface heat flow (Lucazeau, 2019) with the corresponding modelled values. Control point locations are shown in Fig. 3. Only the heat flow observations with the highest qualities (error range between 10% and 20%) were considered. In general, the measured heat flow is lower within the Caribbean Sea (40-80 mW m⁻²) than in the Pacific Ocean (>80 mW m⁻²). Minima (10-40 mW m⁻²) are found close to the area of influence of the Magdalena Fan depocenter (MFD, Fig. 3), likely as a result of the thermal blanketing by the thick sedimentary sequence (Scheck-Wenderoth and Maystrenko, 2013). ¶

Eliminado:)

Con formato: Alemán (Alemania)

Eliminado: computed

Eliminado: explored

Eliminado: . Moreover,

Eliminado: for

Eliminado: zone was computed as the temperature difference between the surface and 20 km

Eliminado: .

Eliminado: 11¶

were included. This is particularly useful in complex tectonic settings such as the study area, where the application of a 1D geotherm approach for calculating the thermal field would not be representative of the present-day configuration.

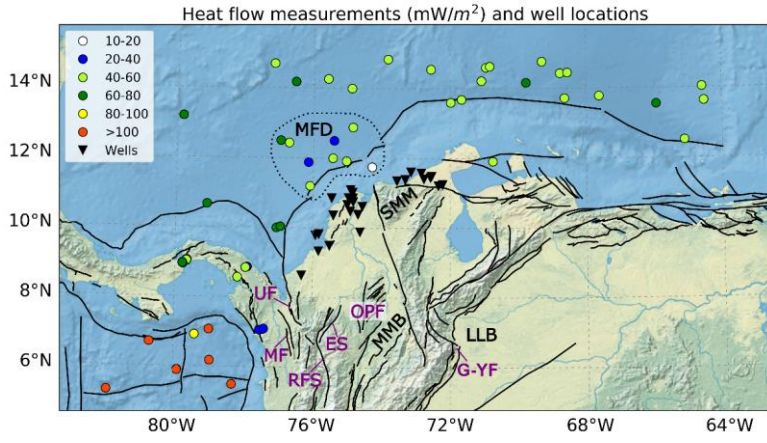


Figure 3. Measurements used for validating the thermal model. Color-coded dots: heat flow values with the highest qualities (Lucazeau, 2019). Black triangles: wells from the oil industry with measured downhole temperatures (ANH, 2020). Active fault traces (black lines) as in Fig. 1a. ES = Espíritu Santo Fault. G-YF = Guaicaramo and Yopal Faults. OPF = Otú-Palestina Fault system. RFS = Romeral Fault System. MF = Murindó Fault. UF = Uramita Fault. The dotted polygon highlights the heat flow values close to the Magdalena Fan depocenter (MFD). Additional features discussed in the text: LLB = Llanos Basin. MMB = Middle Magdalena Basin. SMM = Santa Marta Massif.

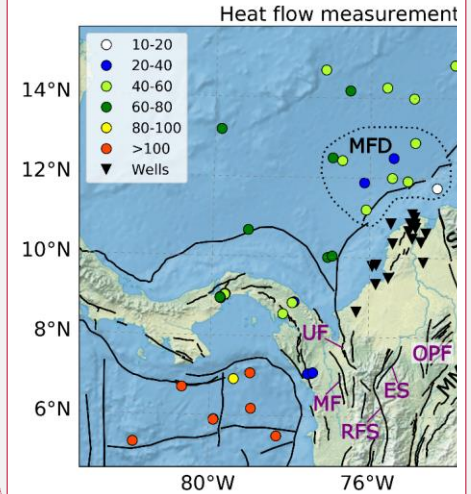
3.2 Crustal seismogenic depths

The crustal seismogenic depths were calculated from the earthquake catalogue, as described below.

3.2.1 Earthquake catalogue

A composite earthquake catalogue was compiled for the study area and surroundings ($\pm 1.5^\circ$ of latitude and longitude), using public sources, with preference given to global databases over national ones. This last choice stems from the study area covering several countries, hindering a proper homogenization of the local catalogues. For each event, the best location source, that is, the one with the most reliable depth, was chosen by using the following order of preference: 1) The gWFM database (Wimpenny and Watson, 2020), based on synthetic body-waveform modeling, and updated to version 1.2, which includes earthquake locations calculated in the region by Wimpenny, (2022) and Wimpenny et al. (2018). 2) Locations calculated by full-waveform modelling (with the ISOLA code; Sokos and Zahradnik, 2008) using records obtained at regional or local distances by the Colombian Geological Survey (Dionicio et al., 2023; Servicio Geológico Colombiano, 2023) and by Quintero et al. (2023). 3) A high-precision hypocentral relocation for the 2008 Quetame mainshock by Diczelis et al. (2016). 4) Locations with free (not fixed) hypocentral depth from the ISC-EHB dataset (Weston et al., 2018; Engdahl et al., 2020), which is compiled and curated by the International Seismological Centre (2023a). And 5) The prime locations reported in the reviewed ISC Bulletin (International Seismological Centre, 2023b) which has been completely rebuilt for the period 1964-2010 (Storchak et al., 2020), adding additional earthquakes and relocating hypocenters with the same location procedures used from 2011 onwards (Bondár and Storchak, 2011). Prime hypocenters are those relocated by ISC, or provided by regional agencies and considered by ISC as the best determined ones (Di Giacomo and Storchak, 2016). The resulting catalogue

Eliminado: A similar approach was followed by Gholamrezaie et al. (2018), and it allows to justify the use of a 3D modelling scheme in which the geological heterogeneities of the system are included. This is particularly useful in complex tectonic settings such as the study area, where the assumption of a 1D geotherm approach will not be representative of the present-day configuration.



Eliminado: measurements

Eliminado: (Lucazeau, 2019).

Eliminado: (ANH, 2020).

Eliminado: 1

Eliminado: measurements

Eliminado: thickness

Eliminado: of the upper and lower stability transitions for seismogenesis, and the

Con formato: Inglés (Estados Unidos)

Eliminado: thickness (given by their difference)

Eliminado: 3.2.1

Con formato: Esquema numerado + Nivel: 3 + Estilo de numeración: 1, 2, 3, ... + Iniciar en: 1 + Alineación: Izquierda + Alineación: 1,27 cm + Tabulación después de: 0 cm + Sangría: 2,54 cm

Eliminado: 12

585 covers the period from January 1980 (when the ISC Bulletin became more homogeneous, e.g.: Woessner and Wiemer (2005) until June 2021 (the last month fully revised in the ISC Bulletin at the time of writing).

590 Most locations in the catalogue were provided either by the ISC-EHB dataset or the reviewed ISC Bulletin. Only for 34 earthquakes, the location was provided by full-waveform inversion. In these cases, the location refers to the centroid (the center of seismic moment release), instead of the hypocenter (where the earthquake rupture starts). This adds some heterogeneity to the catalogue, as these two locations may not be the same for a given earthquake. However, high-precision full-waveform inversion locations are better constrained than hypocentral locations calculated from wave phase arrivals (e.g.: Wimpenny, 2022), and most of these earthquakes had moment magnitude $M_w < 5.0$, with small rupture dimensions, which considering the location uncertainties leads to a negligible difference between the actual hypocentral and centroid location.

595 For each event, a preferred magnitude value was assigned. The original M_w values reported from the sources 1 to 3 in the list above were used for the corresponding earthquakes. For those with locations provided by ISC (sources 4 and 5), M_w was used if reported, preferably from the Global CMT catalogue (Dziewonski et al., 1981; Ekström et al., 2012), or alternatively from other agencies as reported by ISC (Di Giacomo et al., 2021). If no M_w was available, we adopted the hierarchy proposed by ISC for selecting the most reliable, preferred magnitude type (Di Giacomo and Storchak, 2016). Earthquakes without reported magnitudes were disregarded.

600 In order to assess the magnitude of completeness (M_c) of the composite catalogue, we first checked the time series of magnitude values (Fig. S2, e.g.: Gentili et al., 2011; González, 2017). This evidenced that small earthquakes were systematically better detected since June 1993, when regional seismic monitoring improved (Arcila et al., 2020). Therefore, we use this date to split the catalogue into two sub-periods with different mean M_c (calculated with the maximum curvature method, Wiemer and Wyss, 2000; Woessner and Wiemer, 2005): $M_c = 4.6$ from January 1980 to May 1993, and $M_c = 3.5$ from June 1993 – March 2020 (Fig. S3). Spatial variations of M_c within these periods were mapped and considered negligible for our analysis (Text S5).

610 The M_c values for each period were used as minimum thresholds for the subsequent analysis despite in our study we do not investigate the corresponding magnitude-frequency distribution. For a given magnitude, deep earthquakes typically generate smaller amplitudes of ground motion, so they are more difficult to detect by seismometers and preferentially missing in the earthquake catalogues. Indeed, M_c increases with depth when such dependence is quantified (e.g.: Schorlemmer et al., 2010). So, if we would have relied on an incomplete catalogue (considering also earthquakes with magnitude $< M_c$) the statistical results would be biased towards those resulting from shallow earthquakes, which are more likely to be detected and included in the catalogue. Also, the apparent spatial earthquake distribution would be distorted by numerous earthquakes with magnitude $< M_c$ located, e.g. in the vicinity of recording stations. Pruning the catalogue from earthquakes below M_c should avoid such biases.

620 Next, earthquakes with non-reported depths, as well as those with depths reported as 0 km or fixed, or with reported depth error > 15 km were also excluded from the analysis. This selection allowed pruning the worst located earthquakes but preserving a sufficient number of events to perform our analysis. Note that the hypocentral depth errors reported in the ISC or ISC-EHB Bulletin format are wide, since they cover the 90% uncertainty range (Biegalski et al., 1999). The impact of the remaining hypocentral depth uncertainties on the results will be quantified later.

625 The datum (reference surface used as depth=0) in the ISC Bulletin is the WGS84 reference ellipsoid (István Bóndár & Dimitri Storchak, pers. comm., 2020; see also Bóndár and Storchak, 2011). Our thermal model considers sea level as the reference surface, so hypocentral depths were referred to the EGM2008-5 geoid model (Pavlis et al., 2012; Hanagan and Mershon, 2021), which approximates well the sea level in the study area. The reference depth for locations provided by full-waveform inversions was considered as the solid Earth surface (e.g.: Wimpenny, 2022), so their depths below sea level were calculated considering the topo-bathymetry only.

Eliminado: Since the study area covers several countries, a global earthquake catalogue was preferred over national ones. We therefore relied upon the reviewed ISC Bulletin (International Seismological Centre, 2022), regarded as the definitive record of the Earth's seismicity. This catalogue has been completely rebuilt for the period 1964-2010 (Storchak et al., 2020), adding additional earthquakes and relocating hypocenters with the same location procedures used from 2011 onwards (Bóndár and Storchak, 2011). However, for earthquakes occurring before 1980, the ISC Bulletin is still particularly heterogeneous (e.g.: Woessner & Wiemer, 2005). Consequently, we limit our study to the period since 1980. Only prime hypocenters (i.e.: those relocated, or considered as best determined by ISC, see Di Giacomo & Storchak, 2016) were used. At the time of this analysis, the bulletin had been reviewed until March 2020.¶

The ISC Bulletin frequently reports several magnitudes for each event. We chose only those associated with the prime hypocenter, and adopted the hierarchy proposed by ISC for selecting the most reliable, preferred magnitude type (Di Giacomo and Storchak, 2016) (see supplementary material for details). Earthquakes without reported magnitudes were disregarded.¶

The catalogue was analyzed in details (see the supplementary materials), considering the time series of magnitude values (e.g.: Gentili et al., 2011; González, 2017) and a sudden improvement of regional seismic monitoring in June 1993 (Arcila et al., 2020). The latter was used to divide the catalogue into two sub-periods with different mean magnitude of completeness (calculated with the maximum curvature method, Wiemer & Wyss, 2000, Woessner & Wiemer, 2005): $M_c = 4.6$ from January 1980 to May 1993, and $M_c = 3.5$ from June 1993 – March 2020. These magnitude values were used as minimum thresholds for the subsequent analysis.¶ Earthquakes with non-reported depths, as well as

Eliminado: with depths

Eliminado: 0 km or fixed, or

Eliminado: 30

Eliminado: of hypocentral temperature determinations

Eliminado: (Biegalski et al., 1999). The possible

Eliminado: commented on

Con formato: Fuente: 10 pto

Eliminado: 13¶

665 When selecting crustal seismicity, we disregarded earthquakes mislocated above the solid Earth's surface
(according to the GEMMA topographic model, Weatherall et al., 2015), or located below the crust-mantle (Moho)
boundary of the GEMMA model (Reguzzoni and Sampietro, 2015) interpolated to a homogeneous grid of 5 km × 5
670 km. We preferred the GEMMA model over others available in the region (e.g. Avellaneda-Jiménez et al., 2022;
Poveda et al., 2018) because either these studies do not cover the entire study area, or portray large regions with data
gaps, as they relied on available seismic stations. The uncertainty of this model is represented in Fig. S4.

675 The data repository (Gomez-Garcia et al., 2023) provides the catalogue subset of the best located crustal
earthquakes in the study region, selected according to the criteria above, with their calculated hypocentral temperatures
(Sect. 4.3). The histograms of their depth errors are shown in Fig. S5. For this subset, the scalar seismic moment (M_0 ,
in N-m) was calculated (if not already provided by the original sources of the earthquake catalogue), from the standard
IASPEI formula for the moment magnitude M_w (see Bormann, 2015 after Kanamori, 1977). If the preferred magnitude
was not M_w , it was first converted to it using the relations detailed in Text S6: (Di Giacomo et al. (2015, exponential
versions, for body-wave or surface-wave magnitudes), Arcila et al. (2020, for local magnitudes) and Salazar et al.
(2013, for duration magnitudes).

3.2.2 Crustal seismogenic depths and uncertainty quantification

680 A robust statistical estimate of the crustal seismogenic depth at each location requires defining a given
percentile of the observed distribution of nearby reliable earthquake depths. Simply considering the deepest
earthquake (percentile 100%) in the vicinity, despite sometimes used, is not robust, since the available sample of
earthquakes is finite, and future ones will have some chance of being deeper than the deepest ones observed so far. A
more stable statistical measure is the 90% depth percentile, D90 (Marone and Scholz, 1988; Sibson, 1982) of the
685 sample of nearby earthquakes, so that only 10% of them are deeper than this threshold. Indeed, D90 or D95 (the 95%
percentile) are commonly used to define the bottom depth of seismogenic sources in seismic hazard assessments (e.g.:
Bommer et al., 2023). Which of the two percentiles is more statistically meaningful depends on how many earthquakes
are available in the considered sample. A sample of 20 earthquakes suffices to calculate D90 (e.g.: Chiarabba and De
Gori, 2016), so that two of them will be deeper. In contrast, with this sample size, D95 will eventually be less reliable
690 than D90, as it again depends on the deepest earthquake recorded. Larger percentiles, such as 99%, can be used only
if there are many earthquakes in the sample used, such as in high-seismicity regions with dense seismic monitoring
(e.g.: Marone and Scholz, 1988; Marone and Saffer, 2015; Wu et al., 2017; Scholz, 2019).

695 Here, D90 and D95 were spatially mapped considering the subset of crustal earthquakes with the best
hypocentral depth determinations (see previous section). We used the median-unbiased percentile estimator of
Hyndman and Fan (1996) at each node of a latitude-longitude grid with a spacing of 0.1°, considering the closest
earthquakes to each node (at least 20) as the sample dimension for the corresponding D90 and D95 values. The
resolution radius (distance to the furthest earthquake considered in each sample) was set to a minimum of 5 km (in
700 order to cover at least one grid cell of the model). If there were <20 earthquakes within this distance, the radius was
increased up to the 20-th closest earthquake. The percentiles were not calculated for nodes with resolution radius >120
km, where the spatial density of epicentres was deemed too low to obtain reliable results. To avoid boundary effects,
we also considered earthquakes outside the study area, applying the same selection procedure, after checking that M_c
was not larger in this extended region. Given the sample size (20 events), the results based on D90 will be considered
robust and interpreted here, while those of D95 will be only provided as supplementary information.

705 Although this way of spatially sampling the closest earthquakes around each map location is novel for
calculating hypocentral depth percentiles, it has been frequently used for mapping M_c and b -values of the Gutenberg-
Richter distribution (firstly by Wiemer and Wyss, 1997). The reason for our choice is that it maximizes the mapping
detail, that is, the resolution radius will be small in locations with high spatial earthquake density, and large only if
710 necessary, in those locations with sparse seismicity. We avoided the use of a larger earthquake sample for each node,
as it would imply enlarging the resolution radius, considering earthquakes located further away from the nodes, and
thus smoothing out the spatial variations of D90 (or D95).

Eliminado: The reference surface used as depth=0 in the ISC Bulletin is the WGS84 reference ellipsoid (István Bóndár & Dimitri Storchak, pers. comm., 2020; see also Bóndár & Storchak, 2011). Our thermal model considers the actual depth below sea level as reference, so hypocentral depths were referred to the EGM2008-5 geoid model (Pavlis et al., 2012). After this correction, earthquakes located above the solid Earth's surface (within the ocean water column or the atmosphere, according to the GEMMA topographic model, Weatherall et al., 2015) were excluded from our analysis. Such mislocations are the unfortunate consequence of disregarding the actual Earth's topography and bathymetry in the majority of the routine hypocentral depth determinations by ISC (and most seismological agencies). This location problem is emphasized in study areas such as ours, with several kilometers of topographic relief between the ocean bottom and the mountain tops.¶ Since we focus our analysis on crustal seismicity, we also disregarded earthquakes located below the crust-mantle (Moho) boundary, as provided by the GEMMA model (Reguzzoni and Sampietro, 2015), interpolated to a homogeneous grid of 5 km × 5 km. We preferred the GEMMA model over other models available in the region (e.g.: Avellaneda-Jiménez et al., 2022; Poveda et al., 2018) because either these studies do not cover the entire study area, or portray large regions with data gaps, as they relied on available seismic stations. The remaining subset thus only contains the best located, crustal earthquakes in the region (Fig. 1), which will be the ones used for calculating the upper and lower stability transitions (Sect. 3.2.2) and hypocentral temperatures (Sect. 4.2).¶ The scalar seismic moment (M_0 , in N-m) was calculated for this subset, from the standard IASPEI formula for the moment magnitude M_w (see Bormann, 2015 after Kanamori, 1977). If the preferred magnitude from the ISC Bulletin was not already M_w , it was first converted to it using relations detailed in the supplementary materials (Text S6): Di Giacomo et al. (2015, exponential versions, for body-wave or surface-wave magnitudes), Arcila et al. (2020, for local magnitudes) and (Salazar et al., 2013, for duration magnitudes). ¶ (...)

Eliminado: The 10% and 90% depth percentiles (D10 and D90, respectively; Marone & Scholz, 1988; Sibson, 1982) were spatially mapped considering the subset of crustal earthquakes with the best hypocentral depth determinations (see previous section). We used (...)

Eliminado: of a fixed number of

Eliminado: Wiemer & Wyss, 1997).

Eliminado: (epicentral distance to the 20th closest earthquake from the node in our case)

Eliminado: in

Eliminado: The upper threshold of this radius was chosen by inspection of

Con formato: Alemán (Alemania)

Con formato: Alemán (Alemania)

Eliminado: resulting maps, to avoid calculating D10 and D90 in regions where the spatial density of epicentres was too low to obtain reliable results. Further details of the resulting map resolution will be commented on in Sect. 4.4.¶ (...)

Eliminado: was avoided

Eliminado: D10 and

Eliminado: .

Eliminado: 14¶

835 In order to quantify the uncertainty of D90 (and D95) at each node, we relied on a combined Monte Carlo and bootstrap procedure. The Monte Carlo simulation accounts for the uncertainty due to reported errors in earthquake depth determination, while the bootstrap quantifies the uncertainty due to the finite size of the sample. In each of the 200 Monte Carlo runs used, a random depth was assigned for each earthquake. For this, it was assumed that its depth uncertainty followed a Gaussian distribution truncated at the solid Earth surface, with a mean given by the best depth estimate, and a standard deviation such that the reported error covers 90% of the uncertainty range, as stated for the locations provided by ISC (Biegalski et al., 1999), which constitute the bulk of the catalogue. Next, the spatial sampling described above was applied to the randomized set of hypocentres, only if they were located within the crust, according to the local depth of the GEMMA Moho model. Then, for each node, 100 random bootstrap samples (Efron, 1979) were generated out of the corresponding sample with at least 20 depth values. Thus, for each node there was a set of 20,000 (= 200 × 100) values of D90 (or D95) from which the average and standard deviation were calculated.

Eliminado: The temperatures at
Eliminado: depths
Eliminado: D10 and

840 The resulting D90 (and D95) values and their corresponding standard deviations and resolution radii are provided in the data repository (Gomez-Garcia et al., 2023) and discussed further in Sect. 4.4. Due to the spatial sampling method used, in most nodes of the map the calculated D90 (or D95) lies within the crust, but there are some areas where the percentile may be located below the crust (such as in regions with abrupt changes in the Moho depth). Only the crustal D90 or D95 values (i.e. those whose depths are not deeper than the Moho) were considered.

Eliminado: of the map

Eliminado: from the 3D thermal model.
Eliminado: for determining D10 and D90
Eliminado: D10 and

4 Results and discussion

4.1 Thermal model validation

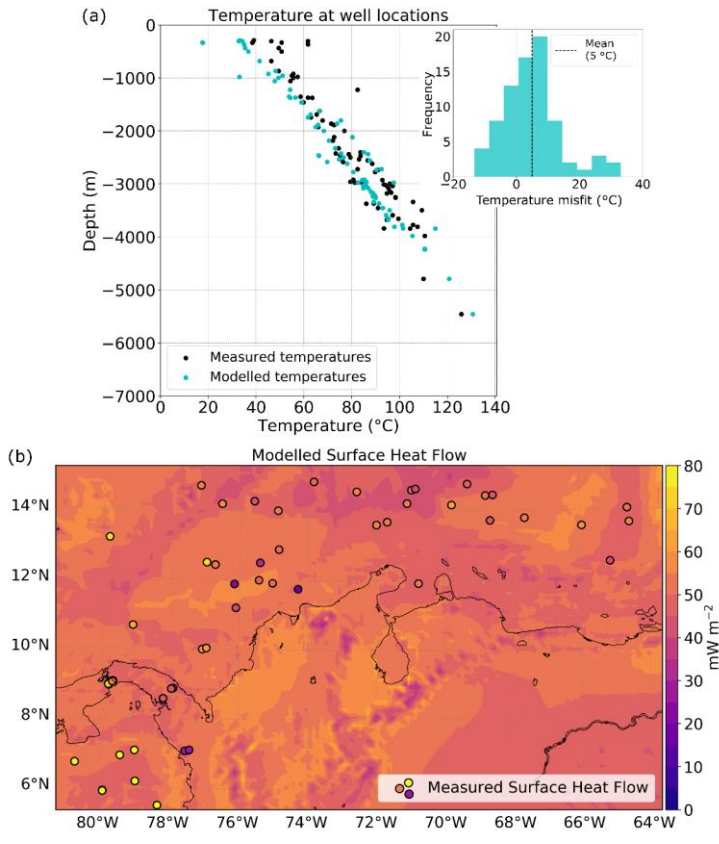
850 In Fig. 4a we compare the modelled and measured temperatures at boreholes (see Fig. 3), based on the selected, best fitting thermal model resulting from the sensitivity test (Text S2). The histogram of residuals (Fig. 4a, right) indicates that most misfits range between -10 and 10°C, with a mean of 5°C, the same magnitude as the common error for borehole temperature estimates. There is a general agreement between modelled temperatures (cyan dots) and measured ones (black dots). However, larger misfits occur at shallower depths (< 1km), which could be explained by shallow advective processes of heat transport (e.g., by groundwater), not considered in our model, especially given the rather small spatial scales at which these processes occur, compared to our regional-scale approach.

Eliminado: lie
Eliminado: in which
Eliminado: s
Eliminado: above or
Eliminado: , respectively (i.e.:
Eliminado: topography/bathymetry or Moho interface). In either case,
Eliminado: nodes lying outside the bounds of our structural model were

860 Figure 4b compares the modelled and observed heat flow values. In general, heat flow measurements are usually affected by local, non-conductive processes of heat transport (such as hydrothermal circulation), making their interpretation difficult in terms of a purely conductive, lithospheric-scale model, as pointed out elsewhere (Scheck-Wenderoth and Maystrenko, 2013; Klitzke et al., 2016). The modelled heat flow is generally lower than the measured one (Fig. 4b), except in the area of influence of the Magdalena Fan (Fig. 3). High observed values in the Pacific Ocean could also be attributed to additional advective heat transport, because they are located in an area of intense faulting (Marcaillou et al., 2006), close to the Panama Fracture Zone. Considering that the associated error in the heat flow data used in this analysis ranges between 10 and 20% (Lucazeau, 2019), it can be concluded that the model fits the regional trend, except in those two areas previously mentioned.

Eliminado: The resulting D10 and D90 values, and their corresponding standard deviations are provided in the data repository (Gomez-Garcia et al., 2022).
Con formato: Alemán (Alemania)
Eliminado: different
Eliminado: In general, there is a good agreement between the modelled temperatures (cyan dots) and the observed ones (black dots).
Eliminado: ; although
Eliminado:). Such a trend
Eliminado: which have
Eliminado: been
Eliminado: .

Eliminado: 15¶



895 **Figure 4.** Validation of the 3D thermal field against measurements of downhole temperatures and surface heat flow. (a) Modelled borehole temperatures show a good agreement with the observed temperatures. The largest misfits (histogram of the right panel) occur at depths shallower than 1km. (b) Calculated surface heat flow (background) and measured values (colored dots, with the same color scale).

4.2 Geothermal gradient: 3D variations and correlation with seismicity

900 Relying on a multi-1D geotherm approach, as commonly done, to compute the thermal field implies a spatially homogeneous setting where lateral variations in heat fluxes, as they do naturally occur, are disregarded. Implications of oversimplifying such three-dimensional interactions via 1D and 2D model representations have been already discussed, for instance, by Cacace and Scheck-Wenderoth (2016).

905 The thermal field within the lithosphere is influenced by factors such as: 1) the imprint from deep mantle sources; 2) the geometries of the different layers that compose the lithosphere; 3) their corresponding thermal conductivities; 4) the heat produced by the radioactive decay of elements present, especially in the (heterogeneous)

- Movido (inserción)[1]**
- Movido (inserción)[2]**
- Eliminado:** The modelled heat flow is generally lower than the measurements, except in the area of influence of the Magdalena Fan (Fig. 4b). The heat flow data in the Pacific Ocean are located in an area of intense faulting (Marcaillou et al., 2006), close to the Panama Fracture Zone; therefore, additional advective heat transport might be responsible for the high measured heat flow values in this region. Considering that the associated error in the heat flow data used in this analysis ranges between 10 and 20% (Lucazeau, 2019), it is possible to conclude that the model fits the regional trend, except in those two areas previously mentioned. Nevertheless, the heat flow data is usually affected by nonconductive processes, such as hydrothermal circulation. For this reason, their interpretation in terms of a purely conductive, lithospheric-scale model is difficult, as other authors have pointed out (Klitzke et al., 2016; Scheck-Wenderoth and Maystrenko, 2013).¶
- 4.2 The need of a 3D thermal approach¶**
- To rely
- Con formato:** Inglés (Estados Unidos)
- Con formato:** Inglés (Estados Unidos)
- Con formato:** Inglés (Estados Unidos)
- Eliminado:** geological
- Con formato:** Inglés (Estados Unidos)
- Eliminado:** the
- Con formato:** Inglés (Estados Unidos)
- Con formato:** Inglés (Estados Unidos)
- Eliminado:** Some implications
- Con formato:** Inglés (Estados Unidos)
- Con formato:** Inglés (Estados Unidos)
- Con formato:** Inglés (Estados Unidos)
- Eliminado:** by Cacace and Scheck-Wenderoth (2016).
- Con formato:** Inglés (Estados Unidos)
- Eliminado:** a variety of
- Eliminado:** 16¶

930 crystalline crust; and 5) the thickness of sedimentary depocenters. Given that all these factors are not homogeneously distributed in space, a 3D thermal approach enables to better resolve all those interactions, while preserving the heterogeneous subsurface configuration.

935 In particular, regional geothermal gradient variations can provide insights about the thermal state of the lithosphere (e.g.: Gholamrezaie et al., 2018). Figure 5a shows the computed geothermal gradient for the regional seismogenic zone (from the surface down to 20 km below it, see Sect. 4.4). Long-wavelength spatial variations are observed both in the oceanic and continental realms, with minima offshore ($13^{\circ}\text{C km}^{-1}$) and maxima underneath the Colombian Andes (up to $23^{\circ}\text{C km}^{-1}$).

940 Moreover, the geothermal gradients can also be used as an indirect indicator of crustal rheology. In Fig. 5a, it is possible to observe the correlation between the spatial distribution of seismicity and the geothermal gradients in this region. The crustal earthquakes occur at locations with a mean geothermal gradient of $19.4 \pm 1.23^{\circ}\text{C km}^{-1}$, preferentially clustering in specific zones, e.g. in the North Andes block and the Panama microplate. Seismicity is almost absent in cold lithospheric areas such as the Guyana craton and the Caribbean Large Igneous Plateau. Such correlation indirectly suggests that in these places, the crust and lithospheric mantle may be strongly coupled, and therefore, the differential stress is not high enough to deform the crust in a brittle regime. This again, is an indication that a 1D geotherm approximation will not be robust enough to model the thermal configuration of the heterogeneous study area.

945 A quantitative measure of the correlation between the spatial distribution of seismicity and the geothermal gradients can be made with the so-called Molchan (or error) diagram (Molchan, 1990, 1991; Molchan and Kagan, 1992), already used to test the skill of geodynamic variables at forecasting the spatial distribution of seismicity (e.g.: Becker et al., 2015).

950 The Molchan diagram (blue curve, Fig. 5b) results from considering all possible thresholds of the geothermal gradient in the map of Fig. 5a, following the procedure proposed by Zechar and Jordan (2008) for continuous 2-D forecast functions. Each point of the diagram shows the fraction of missed events (earthquakes occurred at or below a given threshold) versus the fraction of geographic area of the map covered above that threshold. For example, the lowest gradient at which an earthquake is observed in the map is $15.85^{\circ}\text{C km}^{-1}$; the areas where the gradient is at least at this threshold occupy 84% of the map (fraction of occupied space = 0.84) and below this threshold no earthquake occurred (miss rate = 0). Another example is the threshold at $18.73^{\circ}\text{C km}^{-1}$: exactly 30% of the map area has a gradient larger than this (fraction of occupied space = 0.30), and in those regions 72% of the earthquakes took place (miss rate = $28\% = 0.28$). The lower the threshold of geothermal gradient used, the lower the fraction of missed earthquakes, and the higher the fraction of occupied space.

955 A purely random guess with no skill would yield a curve close to the diagonal shown as a dashed line in Fig. 5b. For example, randomly choosing 20% of the map area should, on average, hit 20% of the earthquakes by chance, and miss 80% of them. A skilful correlation (or forecast) would yield a curve below this diagonal, with larger departures being more statistically significant (Zechar and Jordan, 2008). Fig. 5a contains $N=1969$ crustal earthquakes with well-determined depth (according to the criteria described in sect. 3.2.1), and for such a number, this departure of the curve is indeed statistically significant.

960 The area above the curve can be used as an overall measure of the skill (Zechar and Jordan, 2008). The latter can be quantified by the score S (Becker et al., 2015) given by the area above the Molchan diagram minus 0.5. This exercise with the calculated geothermal gradient yields a score $S=0.261$. Albeit the results from different geographic regions cannot be directly compared, we should note that the value found is similar to those obtained by considering geodynamic variables (i.e.: shear strain rates and rates of topography change), as tested in western North America by Becker et al. (2015). We therefore can conclude that our correlation between the earthquake spatial distribution and the geothermal gradient is physically meaningful, also given that they are variables independent from each other.

975 As the geothermal gradient is a function of the temperatures at given depths (Eq. 2), it changes according to the depth interval used for its calculation; therefore, we explored its variation considering depth intervals of 3 km,

- Eliminado: 3
- Eliminado: ; and 4) the geometries of the different layers
- Con formato: Alemán (Alemania)
- Eliminado: compose the lithosphere. It is therefore likely that
- Con formato: Alemán (Alemania)
- Eliminado: can
- Con formato: Inglés (Estados Unidos)
- Con formato: Inglés (Estados Unidos)
- Con formato: Inglés (Estados Unidos)
- Eliminado: also
- Con formato: Inglés (Estados Unidos)
- Eliminado: In particular, regional geothermal gradient variations can provide insights about the thermal state of the lithosphere (e.g.: Gholamrezaie et al., 2018). Figure 5a shows the computed geothermal gradient for the regional seismogenic zone (from the surface down to 20 km depth), with the temperatures extracted from the 3D thermal model. Long wavelength spatial variations are observed both in the oceanic and continental realms, with minima offshore ($13^{\circ}\text{C km}^{-1}$) and maxima underneath the Colombian Andes (up to $23^{\circ}\text{C km}^{-1}$). Figure 5a also depicts how the selected crustal earthquakes (International Seismological Centre, 2022) occur in tectonic environments with a diverse range of geothermal gradient (...)
- Con formato: Inglés (Estados Unidos)
- Eliminado: Most
- Eliminado: the seismicity
- Eliminado: clusters around
- Eliminado: with geothermal gradients $> 19^{\circ}\text{C km}^{-1}$, i.
- Con formato: Inglés (Estados Unidos)
- Eliminado: terranes
- Eliminado: a
- Eliminado: the latter are
- Eliminado: where
- Eliminado: are
- Eliminado: does
- Con formato: Inglés (Estados Unidos)
- Eliminado: exceed the static crustal strength
- Eliminado: A quantitative measure of the correlation between th (...)
- Movido hacia arriba[1]: Figure 4. Validation of the 3D thermal
- Eliminado: (a) Modelled
- Movido hacia arriba[2]: temperatures show a good agreement

- Eliminado: bar). ¶ (...)
- Con formato: Sangría: Primera línea: 1,25 cm
- Con formato: Inglés (Reino Unido)
- Eliminado: 17¶

from the surface down to 30 km depth (Fig. S6). Besides a general decrease in the geothermal gradient with depth, the most remarkable result is that in the continental realm there is not a constant pattern at all depths. In the elevated Andes mountains, the geothermal gradient reaches its maxima in the uppermost 6 km (Figs. S6a and S6b), but this trend shifts at larger depths, where the highest gradients spatially correlate with thick sedimentary basins (Fig. S7). This behavior is consistent with an increase in the amount of radiogenic heat production associated with the thick crystalline crust of the Andes, and with the thermal blanketing effect of the sediments, which retains heat in the underlying crust (Scheck-Wenderoth and Maystrenko, 2013; Cacace and Scheck-Wenderoth, 2016).

Eliminado: S2... Besides a general decrease in the geothermal gradient with depth, the most remarkable result is that in the continental realm there is not a constant pattern at all depths. In the elevated Andes mountains, the geothermal gradient reaches its maximum in the uppermost 6 km (Figs. S6a and S6b), but this trend shifts at larger depths, where the highest gradients spatially correlate with thick sedimentary basins (Fig. S7).

Con formato

Eliminado: retain heat in the underlying crust (Cacace and Scheck-Wenderoth, 2016; Scheck-Wenderoth and Maystrenko, 2013).

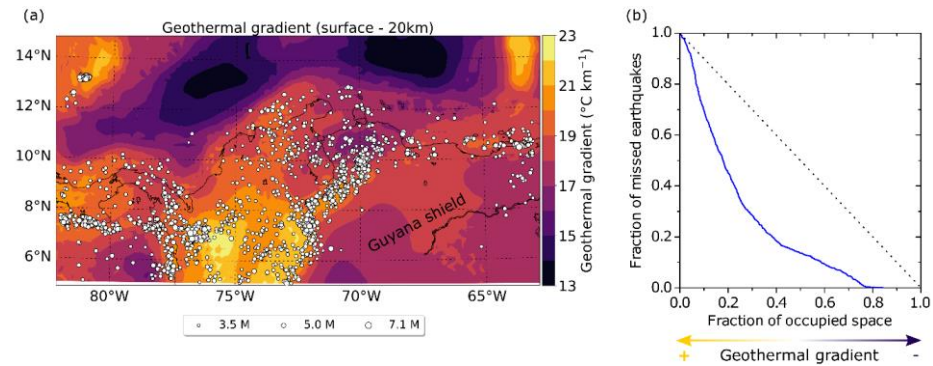


Figure 5. Correlation between geothermal gradient and the spatial distribution of crustal seismicity. (a) Geothermal gradient in the study area computed in the uppermost 20 km of the lithosphere (about the regional average of the crustal seismogenic depth, Sect. 4.3). Large spatial variations are observed both onshore and offshore. White dots: Crustal seismicity analyzed in this study (Sect. 3.2.1). (b) Molchan diagram showing the skill of the spatial distribution of the geothermal gradient at forecasting the distribution of crustal earthquakes.

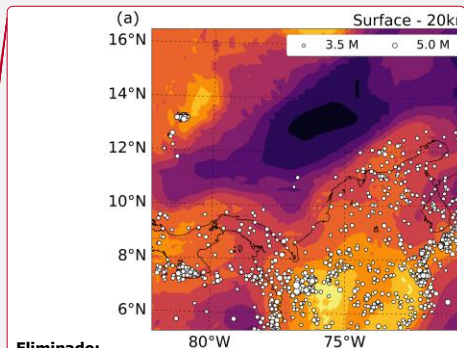


Figure 5. Correlation between geothermal gradient and the spatial distribution of crustal seismicity. (a) Geothermal gradient in the study area computed in the uppermost 20 km of the lithosphere (about the regional average depth of the lower crustal seismogenic depth, Sect. 4.3). Large spatial variations are observed both onshore and offshore. White dots: Crustal seismicity analyzed in this study (Sect. International Seismological Centre, 2022), selected as detailed in Sect. 3.2.1. (b) Molchan diagram showing the skill of the spatial distribution of variations in the geothermal gradient at forecasting the distribution of crustal earthquakes. The dashed diagonal would be the expected result of a random prediction, and a skillful forecast should yield a curve below it.

Eliminado: will

Eliminado: Seismicity is frequent in region 1, as it hosts the Murindó seismic cluster, including the largest earthquake in the selected dataset ($M_w = 7.1$), with a hypocentral depth of 21.1 km (Fig. 1a), and an associated modelled temperature of ~453°C. In the Otú-Palestina and El Espíritu Santo fault systems (region 2), the deepest hypocentral depths in the crust are reported (> 30 km) (Fig. 1a), giving as a result modelled hypocentral temperatures of more than 600°C. In the Venezuelan Andes, bounded by the Boconó Fault (region 3), seismicity is spatially denser than in the rest of the North Andes region, and shows a shallowing pattern from the southwest towards the northeast (Fig. 1a). Such a trend implies a transition from higher hypocentral temperatures close to the Colombian-Venezuelan border towards smaller magnitudes in the Falcon basin (see location of this and other basins in Fig. S7).

Con formato

Con formato: Alemán (Alemania)

Eliminado: colder ones

Con formato: Alemán (Alemania)

Eliminado: .

Eliminado: 18

4.3 Relation between lithology, hypocentral temperature and seismic moment release

The modelled hypocentral temperature distribution of the selected earthquake dataset is shown in Fig. 6. We focus our discussion around the three sub-regions as previously defined in Fig. 1a. Seismicity is frequent in region 1, as it hosts the Murindó seismic cluster, including the largest earthquake in the selected dataset ($M_w = 7.1$), with a hypocentral depth of 21.1 km (Fig. 1a), and an associated modelled temperature of ~453°C. In the Otú-Palestina and El Espíritu Santo fault systems (region 2), the deepest hypocentral depths in the crust are reported (> 30 km) (Fig. 1a), giving as a result modelled hypocentral temperatures of more than 600°C. In the Venezuelan Andes, bounded by the Boconó Fault (region 3), seismicity is spatially denser than in the rest of the North Andes region, and shows a shallowing pattern from the southwest towards the northeast (Fig. 1a). Such a trend implies a transition from higher hypocentral temperatures close to the Colombian-Venezuelan border towards smaller magnitudes in the Falcon basin (see location of this and other basins in Fig. S7).

A synthesis of modelled temperatures for the entire study area is presented in Fig. 7, where we also depict the seismogenic window as typically associated with granite (90-350°C; Blanpied et al., 1992; Scholz, 2019), gabbro (200-600°C; Mitchell et al., 2015; He et al., 2007; Scholz, 2019) and olivine gouge (600-1000°C; King and Marone, 2012; Scholz, 2019). Granitic rocks are typically regarded as the representative lithology in the crystalline continental crust. However, the study area has a variety of allochthonous terranes that have been attached to the margin, including large ophiolite sequences, associated to oceanic plateaus, and magmatic arcs (Fig. 1b) (Montes et al., 2019; Boschman et al., 2014; Kennan and Pindell, 2009); therefore, the seismogenic windows of gabbro and olivine are also considered.

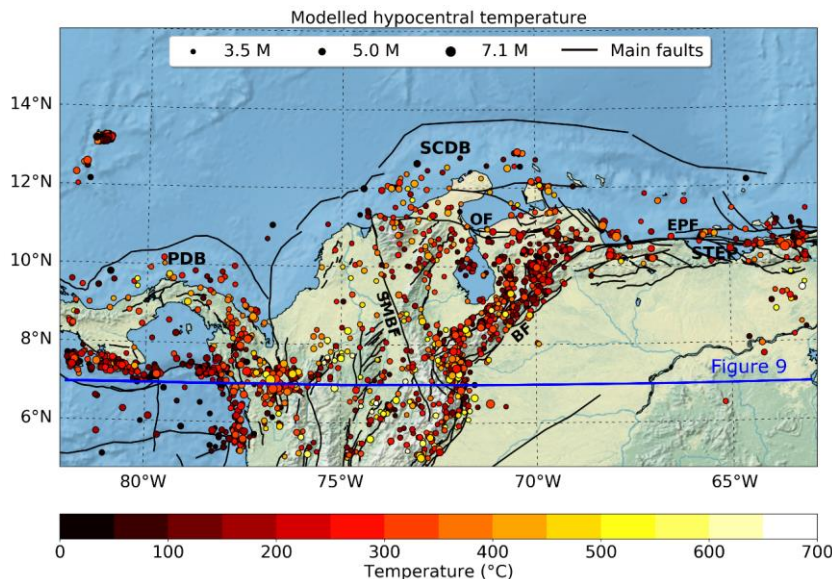


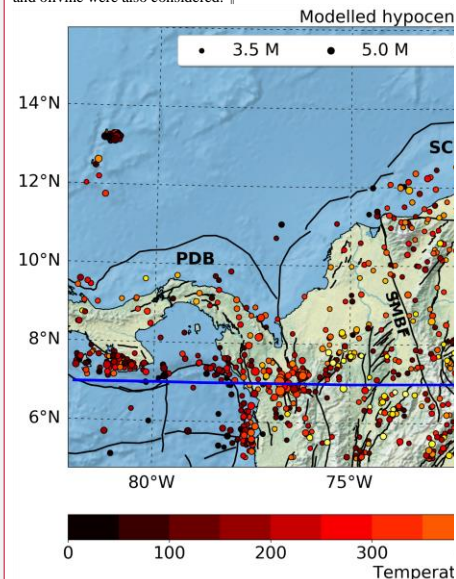
Figure 6. Modelled hypocentral temperature for crustal earthquakes. Acronyms and active fault traces (black lines) as in Fig. 1a. The surface projection of the vertical profile of Fig. 9 is shown as a blue line.

Most crustal earthquakes have hypocentral temperatures of less than 350°C (Fig. 7a), within the observed seismogenic window of granite and/or partially overlapping with that of gabbro (Fig. 7b). Nevertheless, modelled temperatures range from 1°C (offshore events) to almost 700°C, with only 13 events reaching the seismogenic window reported for olivine gouges at > 600°C. Such temperatures support early findings based on laboratory experiments (King and Marone, 2012; Scholz, 2019, and references therein), as well as more recent ones, suggesting that the brittle-to-ductile transition in mantle-forming minerals might occur at higher temperatures (> 600°C) than previously expected (e.g.: Chen et al., 2013; Grose and Afonso, 2013; Ueda et al., 2020).

Despite relying only on the best-located earthquakes (see Sect. 3.2.1), uncertainties in the hypocentral depths still remain (Fig. S5). In any case, the overall trend of hypocentral temperatures is expected to be robust despite these uncertainties, as it is based on almost 2000 events. The hypocentral depths show a unimodal distribution, with the peak at about 5 km (Fig. 7c). Computing D90 associated to the whole catalogue of selected crustal earthquakes results in a regional seismogenic depth for crustal earthquakes of about 20.5 km (blue dotted line in Fig. 7c).

Our analysis indicates that the 18 October 1992 Murindó mainshock (darkest blue dot in Fig. 7b) nucleated close to the regional base of the seismogenic crust (D90), and in particular, at the D90 depth at its location. This behavior supports early findings broadly debated in the literature (e.g.: Tse and Rice, 1986), and suggests that ruptures which initiated within deep and high-stress regions are able to propagate through the entire seismogenic zone and probably reach the surface, resulting in a large rupture area, and therefore, in a large magnitude event. This event dominates the seismic moment release recorded so far in the study area, as can be observed on the seismic moment histogram as a function of depth (Fig. 7d). Its geological effects evidence a surface rupture exceeding 100 km in length (Mosquera-Machado et al., 2009), compatible with the overall rupture length deduced from the source-time functions

Eliminado: A synthesis of modelled temperatures for the entire study area is presented in Fig. 7. Figure 7b also depicts the seismogenic window typically associated with granite (90-350°C), gabbro (200-600°C) and olivine gouge (600-1000°C), according to the review presented by Scholz (2019). Granitic rocks are typically regarded as the representative lithology in the crystalline continental crust. However, the study area has a variety of allochthonous terranes that have been attached to the margin, including large ophiolite sequences, associated to oceanic plateaus, and magmatic arcs (Montes et al., 2019); therefore, the seismogenic windows of gabbro and olivine were also considered. ¶



Eliminado: 1

Eliminado: 10

Eliminado: The majority of the seismic events share

Con formato: Inglés (Estados Unidos)

Con formato: Inglés (Estados Unidos)

Eliminado: few events reaching the seismogenic window reported for olivine gouges at > 600°C. These ranges, however, are not strict because in nature rocks are a mix of different minerals that can contribute to a more complex behavior. For example, mixtures of 65% illite and 35% quartz might exhibit a seismogenic window between 250 and 400°C, while replacing the illite for muscovite implies a new window between 350 and 500°C (see grey dashed line in Fig. 7b) (Scholz, 2019 and references therein).

Eliminado: 19¶

of the earthquake sub-events (Li and Toksoz, 1993) and the size of the aftershock distribution (Arvidsson et al., 2002). Thus, we infer that the mainshock ruptured the whole seismogenic crust, from its base up to the surface.

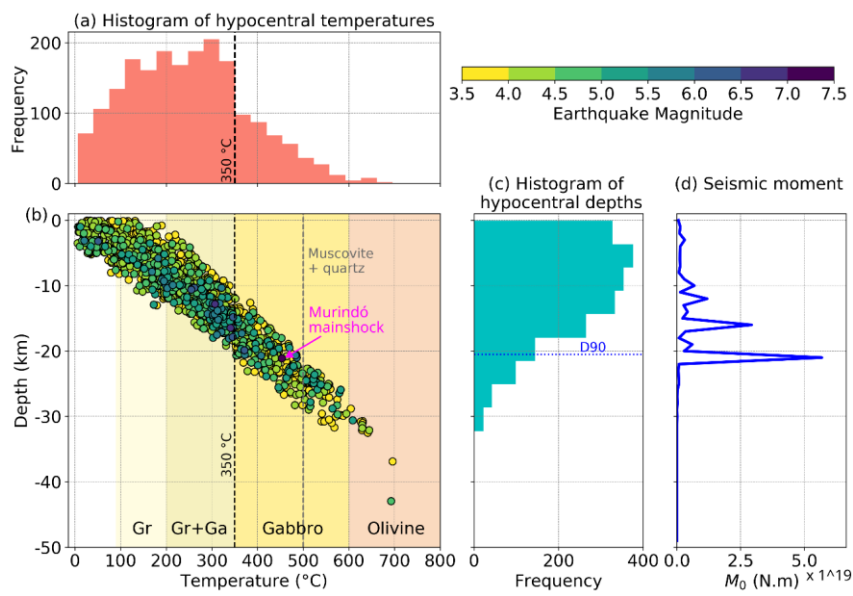


Figure 7. Synthesis of the modelled hypocentral temperatures. (a) Histogram of hypocentral temperatures. (b) Modelled temperature versus depth and preferred magnitude (color coded according to the scale shown in the upper right). Colored domains in the graph represent the seismogenic windows of different rocks or minerals as reported by laboratory experiments (see main text). Gr = Granite. Gr+Ga = shared seismogenic window between granite and gabbro. (c) Histogram of hypocentral depths with regional (average) $D_{90} = 20.5$ km. (d) Histogram of seismic moment release (M_0 , in N.m) as a function of depth, with depth bins of 1 km.

4.4 Depths and temperatures at the base of the seismogenic crust (D90)

The D_{90} depths, the associated temperatures, the D_{90} uncertainty estimates and the resolution radius are shown in Fig. 8. The D_{90} depths vary in space, ranging between 9.8 and 42.7 km, and several abrupt changes can be traced to known crustal structures. Our results suggest a transition from shallow D_{90} depths and cold temperatures associated to oceanic terranes with island arc affinity in western South America, towards deeper and hotter values in terranes with a more sheared continental affinity in the east (blue polygons in Fig. 8b). In particular, in the D_{90} estimates, the Romeral Fault System (RFS, Fig. 3) seems to act as a boundary between the oceanic plateau-like affinity and the sheared continental environment. The latter is characterized by the deepest D_{90} values of NW South America, reaching up to 35 ± 3.5 km (corresponding temperatures $\sim 650^\circ\text{C}$). These maxima within our study region 2 are bounded by the Otú-Palestina and El Espíritu Santo fault systems to the west, and the western thrust front of the Eastern Cordillera to the east. We interpret this trend to be in agreement with the crustal-scale structure that these fault systems likely represent (Kennan and Pindell, 2009) and suggest a significant rheological contrast in the transition between the Central and Eastern Cordilleras, along the Middle Magdalena Basin (MMB, Fig. 1b).

Eliminado: The hypocentral depths show a slightly bimodal distribution, with the largest peak between 0 and 5 km and a secondary one at ~ 10 km (Fig. 7c). Computing the D_{10} and D_{90} associated to the whole catalogue of selected crustal earthquakes results in a regional seismogenic zone ranging on average between 1.8 and 20.9 km. The occurrence of seismicity at very shallow depths (< 2 km) suggests the presence of not well-developed faults in the study area (Scholz, 2019). However, despite relying only on the best located earthquakes (see Sect. 3.2.1), large errors in the hypocentral depths still remain (up to 30 km, see Fig. S5), and should be considered in the analysis of our results. ¶

The largest events ($M > 6.5$) were recorded between 15 km and 20 km depth (dark blue dots in Fig. 7b), close to the lower stability transition (D_{90}). This behavior supports early findings broadly debated in the literature (e.g.: Tse & Rice, 1986), and suggests that ruptures which initiated within deep and high-stress regions are able to propagate through the entire seismogenic zone and probably reach the surface, resulting in a large rupture area, and therefore, in a large magnitude event. In particular, our analysis indicates that this could have occurred in the Murindó sequence in 1992. The two largest events ($M_s = 7.3$ and $M_s = 6.8$) occurred at the base of the seismogenic zone (16.7 km and 15.5 km, respectively), and are dominating the seismic energy release content in the study area, as can be observed on the seismic moment release curve (Fig. 7d). The geological effects of the 18 October 1992 mainshock suggest that it probably caused surface rupture exceeding 100 km in length (Mosquera-Machado et al., 2009), compatible with the overall rupture length deduced from the source-time functions of the earthquake sub-events (Li and Toksoz, 1993) and the size of the aftershock distribution (Arvidsson et al., 2002). Thus, we infer that the mainshock ruptured the whole seismogenic crust, from its base up to the surface. ¶

4.4 Depths and temperatures at the upper and lower stability transitions (D10 and D90)¶

The maps of D_{10} , D_{90} and their temperatures, shown in Fig. 8, evidence spatial variations whose limits can sometimes be traced to known crustal structures. Several patterns can be recognized regarding the computed upper stability transition (D_{10} , Fig. 8a). Close to the Murindó cluster (region 1), the Uramita fault acts as a preferential boundary between deeper the D_{10} values in the Panamá-Chocó block, and shallower ones to the east of the fault, in the northern part of the Western Cordillera. In region 2, D_{10} reaches a local maximum of almost 10 km depth in the Otú-Palestina system. The Venezuelan Andes (region 3) are characterized by relatively homogeneous, shallow values of D_{10} of less than 2 km. The Oca-Ancon fault systems bound deep D_{10} values towards the north of the fault, and shallow values towards the south. ¶

The most remarkable patterns found about the lower stability transition (D_{90} , Fig. 8b) are its deep values associated to the Otú-Palestina and El Espíritu Santo fault systems (region 2). D_{90} depths of almost 35 km in the Otú-Palestina are in agreement with the crustal-scale structure that these systems likely represent (Kennan and Pindell, 2009) and are consistent with significant rheological contrasts in the transition between the Central and Eastern Cordilleras. The D_{90} values in the Venezuelan Andes are clearly bounded by the presence of major faults, reaching shallow depths, (...)

Eliminado: . Different colored

Eliminado: Scholz, 2019

Eliminado: $D_{10} = 1.8$ km and

Eliminado: 9

Con formato: Fuente: 10 pto

Eliminado: 20¶

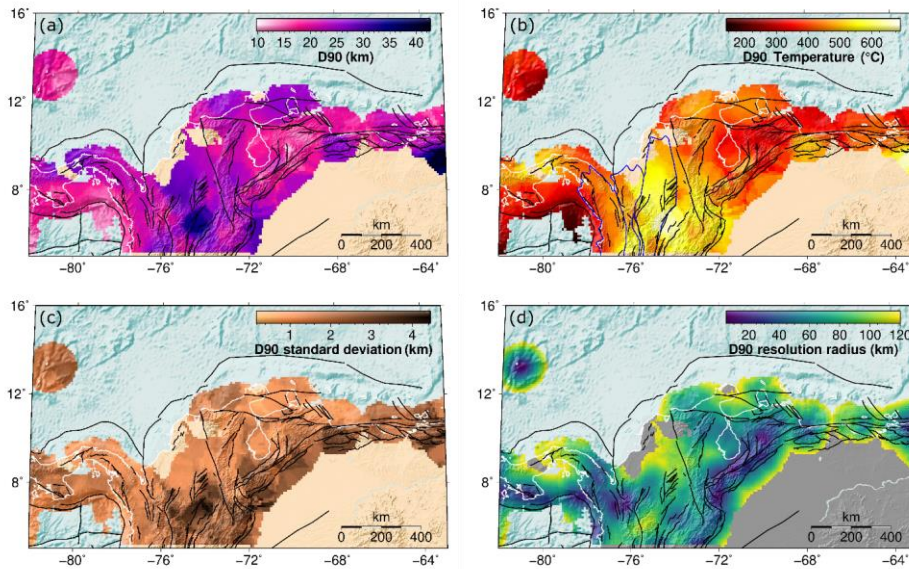


Figure 8. Results on D90, showing how the crustal seismogenic depth, and its associated temperature, varies spatially across the region. (a) D90 depths. (b) D90 temperature. Blue polygons: terranes in NW South America after Boschman et al. (2014) and Kennan and Pindell (2009), as represented in Fig. 1b. (c) Uncertainties in D90. (d) Resolution radius used to compute D90. Black lines: active fault traces, as in Fig. 1a. Coastlines are depicted as white lines.

D90 minima (9.8 ± 1.7 km) are located in the Venezuelan Andes (region 3) bounded by major faults along the Boconó system (BF, Fig. 1a). The associated temperatures indicate a transition from hot (deep) CSD in the SW of this region towards colder (shallower) values in the NE. In northern South America, the Oca-Ancon and El Pilar strike-slip faults (OF and EPF, Fig. 1a) seem to separate (to the north and south) tectonic blocks with diverse D90 depths and associated temperatures, suggesting a different rheological behavior. In fact, this margin was also highly affected by the C-LIP migration (e.g.: Boschman et al., 2014).

Our results suggest that the temperatures at the base of the seismogenic crust in the continental realm span a relatively wide range (143°C to 690°C). In most of the study area, we found values larger than those reported as the onset of quartz plasticity (~300°C, Zielke et al., 2020) and in some cases larger than the temperature range consistent with quartz ductile behavior ($350 \pm 100^\circ\text{C}$ – see a detailed review by Chen et al., 2013). The D90 temperatures are also higher than the seismogenic window of rocks and mineral assemblies typically found in the continental crust (see Fig. 7 and Sect. 4.3), especially in region 2, which includes sutures of different (ultra)mafic, C-LIP related terranes (see Sect. 2).

The general patterns previously described are also present in the resulting D95 depths and estimated temperatures, although with a different range (12.4 km to 43, 9 km and 208 °C to 720 °C, respectively, Fig S8). The calculated uncertainties of D90 and D95 (due to the hypocentral depth errors and the size of the available sample of earthquakes) are very similar to each other (Fig. S9). The mean standard deviation of D90 is only 1.8 km (as for D95)

415 and the maximum is 4.4 km (5.0 km for D95). Differences between D95 and D90 are found to be of little statistical significance overall, since, in most cases, these percentiles are between 1.0 and 1.5 standard deviations from one another. Such results indicate that the calculated D90 values are a robust proxy to the SCD.

420 Moreover, uncertainties in D90 (or D95) are similar to (or even smaller than) independent estimates of the Moho depth uncertainties (Fig. S4), evidencing that the estimation of D90 (and D95) is robust given all available data. The errors associated with the Moho geometry (Fig. S4) are significant across the Nazca and South American realms, resulting in uncertainties about the location of the events either in the lithospheric mantle (including both the mantle wedge and the subducting slab), or in the lower continental crust.

425 The spatial resolution of the D90 results highly depends on the spatial density of available earthquakes. This can be observed in the resolution radius map (Fig. 8d), which shows the search radius required for reaching a minimum of 20 seismic events to compute D90. As we allowed a maximum radius of 120 km, the map is truncated at this value. It is possible to observe how regions with dense seismicity required a small radius for reaching the 20 events, including the Murindó cluster (region 1) and the Venezuelan Andes (region 3).

430 Figure 9 shows a longitudinal profile along 7°N (see Fig. 6 for spatial location). Here, it is possible to observe the thermal response of the system, considering the spatially heterogeneous lower boundary condition at 75 km depth. Underneath the Pacific Ocean, the 600°C isotherm bounds the majority of the seismic events located within the crust and uppermost mantle (black filled and open dots), as previously suggested by Chen and Molnar (1983) and McKenzie et al. (2005), while the isotherm gradually shifts upward underneath western South America.

435 The thermal structure of the continental realm is usually more complex than that of the oceanic lithosphere. Our results suggest that the lithospheric mantle underneath the Colombian Andes is hotter than the surroundings, as indicated by a shallowing of the 600°C isotherm (Fig. 9). As a response, most of the crustal seismicity there preferentially occurs at shallower depths.

440 Nevertheless, deep events below the Moho interface (open dots) are also present in this area, especially associated to the Coiba (Nazca) slab, and perhaps the mantle wedge. Although direct estimations of the Moho depth are available at specific locations in the study area (Poveda et al., 2015; Avellaneda-Jiménez et al., 2022), given the regional scope of our analyses, as already noted, we preferred to use the Moho of the GEMMA model (Reguzzoni and Sampietro, 2015). Considering the uncertainties in the hypocentral depths, and also in the Moho estimates (up to ~7 km along this profile), it is especially challenging to make a clear statement about these upper mantle events. However, we can hypothesize that the subducting Coiba plate can host such intraplate events. Alternatively, the occurrence of upper mantle earthquakes is nowadays broadly recognized (e.g.: Chen et al., 2013) as also dehydration reactions can trigger seismicity at temperatures above the normal brittle-ductile transition (e.g.: Bishop et al., 2023; Rodriguez Piceda et al., 2022).

450 Two regions with prominent seismic activity at a crustal scale are recognized: the suture of the Panamá-Chocó block ("Greater Panama" terrane) with NW South America, around the Murindó cluster; and close to the Guaicaramo and Yopal faults (G-YF, Fig. 3), the boundary between the North Andes block (Eastern cordillera) and the Guyana shield. As previously mentioned, along this profile, most of the seismic activity in these areas is bounded by the 600°C isotherm.

455 Variations of the base of the seismogenic crust (magenta dotted line in Fig. 9) are not necessarily correlated with variations in Moho depths. Between ~74°W and ~76°W (approximately corresponding to region 2, Fig. 1a), there is an abrupt deepening of D90, which correlates with a thick lower crust and with the shallowing of the 600°C isotherm due to the thermal imprint of a hot upper mantle. This deepening of D90 causes its correspondingly high temperatures in region 2, as already discussed. Again, to explain that crustal earthquakes occur down to deeper locations despite of the hot lower crust, it is necessary to hypothesize that the latter has a mafic composition, with a deeper brittle-ductile

Eliminado: The temperatures along the D10 surface (Fig. 8c) are highly influenced by a topographic effect. Their maximum values correlate spatially to elevated mountainous areas in the Andes and the Santa Marta massif (SMM, Fig. 3), with a few exceptions north of the Oca-Ancon fault. The temperatures along the D90 surface (Fig. 8d), on the other hand, do not depict such strong correlation with topography. Instead, the hottest domains are associated to sedimentary basins (Fig. S3) and correspond to the deepest values of D90, i.e.: underneath the Otú-Palestina and El Espíritu Santo fault systems (region 2), influenced by the Middle Magdalena basin (MMB, Fig. 3), and beneath the Eastern Venezuelan and the Llanos basins (LLB, Fig. 3).
Our results suggest that the LST in the continental realm occurs over a wide range of temperatures, and in most of the study area, with values larger than those reported as the onset of quartz plasticity (~300°C, Zielke et al., 2020) and in some cases larger than the temperature range consistent with ductile behaviour (350±100°C – see a detailed review by Chen et al., 2013). The D90 temperatures are also higher than the seismogenic window of rocks and mineral assemblies typically found in the continental crust (see Fig. 7 and Sect. 4.2).

Given our results above, we should also notice the following points: 1) there are still large uncertainties in the selected events used in this study (up to 30 km) that could strongly influence the resulting D10 and D90 values; 2) the best-located earthquake dataset has a relatively small number of events, limiting the spatial resolution of the seismogenic thickness calculation (as discussed further in Sect. 4.5); 3) the dataset includes aftershocks (as otherwise the number of events for analysis would be further reduced), which may nucleate at depths larger than the base of the background seismogenic zone (e.g.: Zielke et al., 2020), so the calculated D90 values may be affected by transient deepening of the LST during aftershock sequences; 4) the diverse lithology of the allochthonous terranes accreted to NW South America includes ultramafic, olivine-rich rocks, and therefore, could generate seismicity at temperatures larger than the seismogenic windows of granites and gabbros; 5) a thick lower crust together with a relatively hot upper mantle could contribute to large hypocentral temperatures (Sect. 4.5); and, 6) it is necessary to have more control points within the continental region to constrain the thermal model, as a particular lithology may have a wide range of radiogenic heat production and thermal conductivity values (e.g.: Vilà et al., 2010).

Eliminado: (including both D10 and D90)

Eliminado: available for their calculation

Eliminado: 9b

Eliminado: in the calculation of D10 and

Eliminado: The sources of error in the calculation of the CST are diverse, and include uncertainties in the Moho depths, as well as errors in the earthquake hypocentral depths. The errors associated with the Moho geometry (Fig. S8) are higher across the Nazca and South American realms, resulting in uncertainties about the location of the events either in the lithospheric mantle (including both the

Eliminado: ,

Eliminado: terranes

Eliminado: In these regions, the seismogenic thickness and the depths to the upper and lower stability transitions do not show any direct spatial correlation with variations in Moho depth. However, the seismogenic crust is thicker and deeper where the largest depocenters are present, that is, beneath the Middle Magdalena (MMB) and the Llanos basins (LLB).

Eliminado: 22¶

transition. As mentioned in Sect. 4.3, this profile shows the close proximity of the 1992 Murindó's mainshock hypocenter (cyan star) to the base of the seismogenic crust.

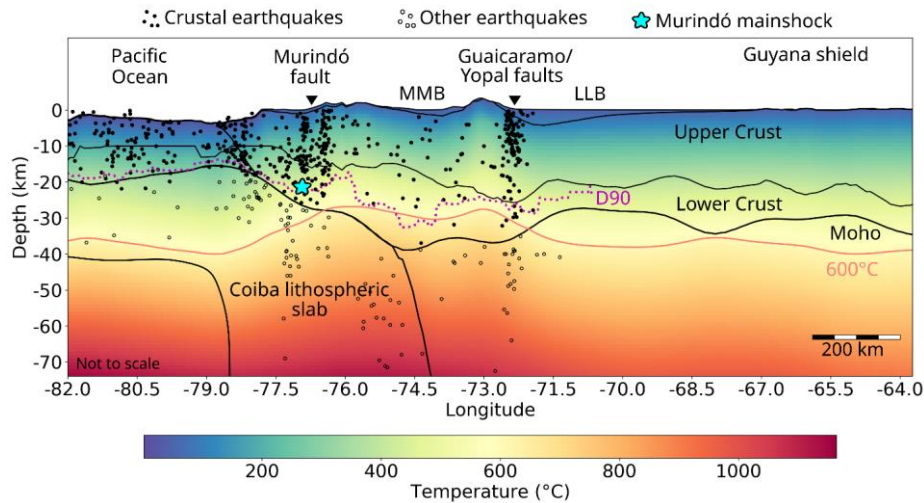


Figure 9. W-E profile at 7°N (see location in Fig. 6) showing the modelled temperatures and their relation to the lithospheric structure, topography and seismicity. Vertical exaggeration 8.5X. Black lines: Boundaries of the lithospheric layers of the structural model as integrated by Gómez-García et al., (2020, 2021). Pink continuous line: 600°C isotherm. Magenta dotted line: D90. Black filled dots: Crustal earthquakes used in this study. Open dots: Earthquakes deeper than the Moho interface, not used for calculating D90. The earthquakes projected in the profile include those from 6.5°N to 7.5°N. Cyan star: Hypocenter of the largest earthquake (Murindó mainshock). LLB = Llanos Basin. MMB = Middle Magdalena Basin (which spatially corresponds to region 2).

Regarding the occurrence of crustal earthquakes at temperatures higher than the seismogenic windows expected for typical crustal rocks, it can be remarked that: 1) The earthquake dataset includes aftershocks (as otherwise the number of events for analysis would be further reduced), which may nucleate at depths larger than the base of the background seismogenic zone (e.g.: Zielke et al., 2020). Thus, the calculated D90 values may be affected by transient deepening of the seismogenic crust during aftershock sequences. These deeper values would yield a larger temperature for the CSD than the long-term one. 2) The diverse allochthonous terranes accreted to NW South America, and the variety of autochthonous crustal blocks, include (ultra)mafic, olivine-rich rocks, which could host seismicity at larger temperatures. 3) The lower crust under part of the Andes may be mafic, able to host earthquakes at the relatively high modelled temperatures, which are due to a hot upper mantle together with a thick upper crust (which generates additional heat due to the decay of radioactive elements, Vilà et al., 2010).

5 Summary and conclusions

We present a three-dimensional, data-integrative model of the thermal field in the north Andean region and the transition to the Caribbean, which displays spatial temperature variations that would have been overlooked by simplified 1D or 2D models. The model fits the available observations of borehole temperatures, and approximates the first-order trend of heat flow values.

Eliminado: In particular, the abrupt deepening of D90 between ~74°W and 76°W spatially correlates with a thick lower crust and with a shallowing of the 600°C isotherm, suggesting that a mafic crust able to host deeper earthquakes (deeper BDT) together with a hot upper mantle could contribute to the the observed increase in hypocentral temperatures in region 2, underneath the MMB. The main shock of the Murindó sequence in 1992 is depicted with a magenta star, and its proximity to the base of the seismogenic crust (D90) is evident.¶

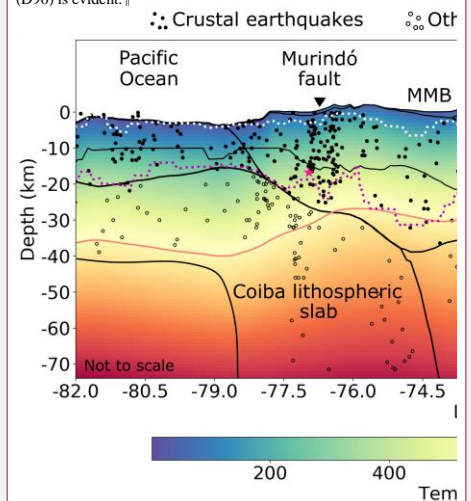


Figure 10. W-E profile at 7°N (see location in Fig. 6) showing the modelled temperatures and their relation to the lithospheric structure, topography and seismicity. Vertical scale exaggerated. Black lines: Boundaries of the lithospheric layers of the structural model as integrated by Gómez-García et al., (2020, 2021). Pink continuous line: 600°C isotherm. Dotted lines: Depths to the upper and lower stability transitions (white: D10 and magenta: D90, respectively). Black filled dots: Crustal earthquakes used in this study. Open dots: Earthquakes deeper than the Moho interface, not used for calculating D10 or D90. The earthquakes projected in the profile include those from 6.5°N to 7.5°N. Star: Hypocenter of the largest earthquake (Murindó mainshock). LLB = Llanos Basin. MMB = Middle Magdalena Basin (which spatially corresponds to region 2).¶

Eliminado: 23¶

This modelling workflow provides an opportunity to compare limiting temperatures for seismogenesis provided by laboratory experiments against real-case scenarios, by considering geological complexities, including a realistic lithospheric structure and the mantle imprint on crustal temperatures.

We have mapped the variable crustal seismogenic depth (CSD) in the region, based on an earthquake catalogue compiled from global sources. The sampling procedure used allows to identifying the variations of the CSD with greater detail in areas with higher spatial earthquake density. Some of those variations are shown to correlate with crustal-scale faults in the region, which acts as tectonic boundaries for crustal domains with different seismogenic behaviors.

Most crustal seismic events in the study area have modelled hypocentral temperatures $< 350^{\circ}\text{C}$, and are located at depths < 20 km. Although most of the hypocentral temperatures range in the reported seismogenic window of rocks and mineral assemblages typically found in continental crust, some of the deepest hypocenters have associated temperatures $> 600^{\circ}\text{C}$, reaching the seismogenic window of olivine. We suggest that the diverse allochthonous crustal blocks, which have been attached to the NW South American margin, and which include large ophiolite sequences, contain olivine-rich, ultramafic rocks, thus explaining these deeper earthquakes. Alternatively, these high-temperature events can be explained by a thick, mafic lower crust (deeper brittle-ductile transition), a hot upper mantle, or by the depth uncertainties of the Moho (up to 7 km in the study area) and those of the hypocenters, which could imply that some of those events actually occurred in the upper mantle. The overall coherence of the calculated hypocentral temperatures with those expected from laboratory measurements provides additional, indirect support to the model, and vice versa.

We additionally found that the spatial distribution of seismicity strongly correlated with the geothermal gradients in the uppermost 20 km of the lithosphere. The Molchan diagram indicates that the geothermal gradient may be as skillful at forecasting the spatial distribution of seismicity as other geodynamic indicators (i.e. strain rates) usually adopted in previous studies. To our knowledge, this skill test had not previously been quantified elsewhere, so we encourage further studies in other regions to explore the systematic nature of the correlation found in our analysis.

Our results evidence that the rupture of the largest event in the region since 1980 ($M_w = 7.1$, Murindó sequence of 1992) propagated from the base of the crustal seismogenic zone. This highlights the importance of considering this transition while defining the lower boundary of seismogenic sources in any seismic hazard assessment.

The estimated CSD in the Otú-Palestina and El Espíritu Santo fault systems is one of the deepest in the study area (up to $\sim 35 \pm 3.5$ km), as most of the deepest events have been recorded beneath these regions. This suggests that these fault systems likely behave as crustal-scale structures, which might have the potential of rupturing large fault areas, thus likely resulting in large-magnitude, hazardous events.

Future analysis will benefit from improved and enlarged thermal and seismic datasets. Additional measurements of heat flow and borehole temperatures (especially within the continent) would better constrain the thermal model. Moreover, as time passes and new seismic stations are installed, more earthquakes are being recorded (particularly of smaller magnitudes than those considered in the present study, $M < 3.5$) with improved depth accuracy. Therefore, uncertainties in hypocentral locations and on the crustal seismogenic depths (and associated temperatures), could be eventually reduced.

Data availability

The results of this publication are available in the data repository Gómez-García et al. (2023). It includes the calculated 3D thermal model, the catalogue of selected earthquakes with their modelled hypocentral temperatures, geothermal gradient and seismic moment, and the mapped depths, uncertainties and temperatures of the CSD (D90 and D95).

Eliminado: We have mapped the depth to the upper (D10) and lower (D90) earthquake stability transitions, and the CST in NW South America, considering only crustal seismicity. This approach allows focusing on the seismogenic properties of the crust, with a sampling procedure which allows identifying variations with greater detail in areas with higher spatial earthquake density. Some of those variations are shown to correlate with crustal-scale faults in the region, which consequently bound crustal domains with different seismogenic behaviors. Our calculations are limited by the completeness of the earthquake catalogue, and the precision of the hypocentral locations. They could be eventually refined in future analyses, as new seismic stations are installed and more earthquakes are being recorded, particularly of smaller magnitudes than those considered here ($M < 3.5$).
The presented three-dimensional approach for calculating of the thermal field allows retrieving spatial variations which would have

Con formato: Alemán (Alemania)

Eliminado: where the ...eological complexities are taken into account... including a realistic lithospheric structure and the mant

Con formato: Alemán (Alemania)

Eliminado: Additional measurements of heat flow and borehole temperatures will eventually help constraining and validating the

Eliminado: Since

Con formato:

Eliminado: including...large ophiolite sequences, they may contain olivine-rich, ultramafic rocks, thus explaining able to host

Con formato: Alemán (Alemania)

Eliminado: either ... thick, mafic lower crust (deeper brittle-ductile transition)...a hot upper mantle, or by the depthlarge...uncertain

Con formato: Inglés (Reino Unido)

Eliminado: The ...patial distribution of seismicity strongly correlated with the geothermal gradientsvariation...in the geother

Con formato: Alemán (Alemania)

Eliminado: to our knowledge, and similar tests would be worth performing...in other regions in order

Con formato: Alemán (Alemania)

Eliminado: check if it is

Con formato: Alemán (Alemania)

Eliminado: .

Eliminado: s...of the two...largest eventevents that occurred...in the region since 1980 ($M_w, M_s = 6.8$ and $M_s = 7.1, 3$), pertaining to

Eliminado: seismogenic thickness...in the Otú-Palestina and El Espíritu Santo fault systems is one of the deepestlargest...in the st

Con formato: Alemán (Alemania)

Eliminado:

Eliminado: Lastly, the seismogenic crust is thicker and hotter below the thick Middle Magdalena basin, suggesting that the ther

Eliminado: 2... It includes the calculated 3D thermal model, the catalogue of selected earthquakes with their modelled hypocentral

Eliminado: 24

885 The thermal calculations were computed using the software GOLEM (Cacace and Jacquey, 2017) available at Jacquey and Cacace (2017). The figures were created using diverse Python packages (Python Software Foundation, Python Language Reference, version 2.7, available at <http://www.python.org>) and GMT (Wessel & Smith, 1991).

Author contribution

1890 AMG developed the research idea, processed the data, performed the thermal calculations and wrote the manuscript. AGG contributed to the research idea, compiled the earthquake catalogue, calculated the crustal seismic depths, and wrote the manuscript. MC developed the software GOLEM and provided support for the thermal calculations. MS and GM supervised the implementation of the thermal calculations. All authors contributed to the discussion and interpretation of the results, revised the manuscript and were partially responsible for obtaining the financial support to develop this research.

Competing interest

The authors declare that they have no conflict of interest.

1895 Acknowledgments

AMGG was partially supported by grants from the German Academic Exchange Service (DAAD, 57314023 and 57440918), the Corporation Center of Excellence in Marine Sciences (CEMarin), Fundación para la Promoción de la Investigación y la Tecnología (Banco de la República de Colombia), the Centre de Recerca Matemàtica (CRM) in Barcelona and the ESM-project of the Helmholtz Impulse and Networking Funds. Grants from MCIN/AEI/10.13039/501100011033, and NextGenerationEU/PRTR were also granted to AMGG (FJC2021-047434-I) and ÁG (FEDER, IJC2020-043372-I and PID2021-125979OB-I00). AMGG is grateful to Antoine Jacquey for his advice during early versions of the thermal models and with Maximilian Frick for his guidance on the use of Paraview. We would like to acknowledge the contributions of Sam Wimpenny and an anonymous reviewer for their constructive feedback.

1905 References

Acosta, J., Velandia, F., Osorio, J., Lonergan, L., and Mora, H.: Strike-slip deformation within the Colombian Andes, *Geol Soc Spec Publ*, 272, 303–319, <https://doi.org/10.1144/GSL.SP.2007.272.01.16>, 2007.

ANH. Banco de información petrolera: https://www.anh.gov.co/Banco_de_informacion_petrolera/EPIS/Paginas/default.aspx, last access: 21 March 2020.

1910 Arcila, M., García, J., Montejo, J., Eraso, J., Valcarcel, J., Mora, M., Viganò, D., Pagani, M., and Díaz, F.: Modelo nacional de amenaza sísmica para Colombia, <https://doi.org/10.32685/9789585279469>, 2020.

Arvidsson, R., Boutet, J. T., and Kulhanek, O.: Foreshocks and aftershocks of the Mw=7.1, 1992, earthquake in the Atrato region, Colombia, *J Seismol*, 6, 1–11, 2002.

Eliminado: The thermal calculations were computed using the software GOLEM (Cacace and Jacquey, 2017) available at Jacquey & Cacace (2017). The figures were created using diverse Python packages (Python Software Foundation, Python Language Reference, version 2.7. Available at <http://www.python.org>) and GMT (Wessel & Smith, 1991).
Author contribution¶
AMG developed the research idea, processed the data, performed the thermal calculations and wrote the manuscript.

Eliminado: processed

Eliminado: data

Eliminado:

Eliminado: with

Eliminado: 25¶

Audemard, F. A. M.: Paleoseismicity studies on the Oca-Ancón fault system, northwestern Venezuela, *Tectonophysics*, 259, 67–80, [https://doi.org/10.1016/0040-1951\(95\)00144-1](https://doi.org/10.1016/0040-1951(95)00144-1), 1996.

930 Avellaneda-Jiménez, D. S., Monsalve, G., León, S., and Gómez-García, A. M.: Insights into Moho depth beneath the northwestern Andean region from gravity data inversion, *Geophys J Int*, 229, 1964–1977, <https://doi.org/10.1093/gji/ggac041>, 2022.

Becker, T. W., Lowry, A. R., Faccenna, C., Schmandt, B., Borsa, A., and Yu, C.: Western US intermountain seismicity caused by changes in upper mantle flow, *Nature*, 524, 458–461, <https://doi.org/10.1038/nature14867>, 2015.

935 Biegalski, K. F., Bohlin, J., Carter, J. A., Coyne, J., Dompierre, D., Novosel, G., and Rinehart, C.: Formats and protocols for messages – IMS1.0. International Data Center & Science Applications International Corporation. Document SAIC-99/3004., 1999.

Bishop, B. T., Cho, S., Warren, L., Soto-Cordero, L., Pedraza, P., Prieto, G. A., and Dionicio, V.: Oceanic intraplate faulting as a pathway for deep hydration of the lithosphere: Perspectives from the Caribbean, *Geosphere*, 19, 206–234, <https://doi.org/10.1130/GES02534.1>, 2023.

940 Blanpied, M. L., Lockner, D. A., and Byerlee, J. D.: An earthquake mechanism based on rapid sealing of faults, *Nature*, 358, 574–576, <https://doi.org/10.1038/358574a0>, 1992.

Bommer, J. J., Ake, J. P., and Munson, C. G.: Seismic Source Zones for Site-Specific Probabilistic Seismic Hazard Analysis: The Very Real Questions Raised by Virtual Fault Ruptures, *Seismological Research Letters*, 94, <https://doi.org/10.1785/0220230037>, 2023.

945 Bondár, I. and Storchak, D.: Improved location procedures at the International Seismological Centre, *Geophys J Int*, 186, 1220–1244, <https://doi.org/10.1111/j.1365-246X.2011.05107.x>, 2011.

Bormann, P.: Are new data suggesting a revision of the current M_w and M_e scaling formulas?, *J Seismol*, 19, 989–1002, <https://doi.org/10.1007/s10950-015-9507-y>, 2015.

950 [Boschman, L. M., van Hinsbergen, D. J., Torsvik, T. H., Spakman, W., and Pindell, J. L.: Kinematic reconstruction of the Caribbean region since the Early Jurassic, *Earth Sci Rev.* 138, 102–136, <https://doi.org/10.1016/j.earscirev.2014.08.007>, 2014.](#)

[Cacace, M. and Jacquy, A. B.: Flexible parallel implicit modelling of coupled thermal-hydraulic-mechanical processes in fractured rocks, *Solid Earth*, 8, 921–941, <https://doi.org/10.5194/se-8-921-2017>, 2017.](#)

955 [Cacace, M. and Scheck-Wenderoth, M.: Why intracontinental basins subside longer: 3-D feedback effects of lithospheric cooling and sedimentation on the flexural strength of the lithosphere, *J Geophys Res Solid Earth*, 121, 3742–3761, <https://doi.org/10.1002/2015JB012682>, 2016.](#)

[Chen, W.-P. and Molnar, P.: Focal depths of intracontinental and intraplate earthquakes and their implications for the thermal and mechanical properties of the lithosphere., *J Geophys Res.* 88, 4183–4214, <https://doi.org/10.1029/jb088ib05p04183>, 1983.](#)

960 [Chen, W. P., Yu, C. Q., Tseng, T. L., Yang, Z., Wang, C. yuen, Ning, J., and Leonard, T.: Moho, seismogenesis, and rheology of the lithosphere, *Tectonophysics*, 609, 491–503, <https://doi.org/10.1016/j.tecto.2012.12.019>, 2013.](#)

[Chiarabba, C. and De Gori, P.: The seismogenic thickness in Italy: constraints on potential magnitude and seismic hazard, *Terra Nova*, 28, 402–408, <https://doi.org/10.1111/ter.12233>, 2016.](#)

965 [Copernicus Climate Change Service \(C3S\). \(2019\). C3S ERA5-Land reanalysis. Copernicus Climate Change Service. <https://doi.org/10.24381/cds.68d2bb30>](#)

[Craig, T. J., Copley, A., and Jackson, J.: Thermal and tectonic consequences of India underthrusting Tibet, *Earth Planet Sci Lett*, 353–354, 231–239, <https://doi.org/10.1016/j.epsl.2012.07.010>, 2012.](#)

[Currie, C. A. and Copeland, P.: Numerical models of Farallon plate subduction: Creating and removing a flat slab, *Geosphere*, 18, 476–502, <https://doi.org/10.1130/GES02393.1>, 2022.](#)

- 1970 [Dicelis, G., Assumpção, M., Kellogg, J., Pedraza, P., and Dias, F.: Estimating the 2008 Quetame \(Colombia\) earthquake source parameters from seismic data and InSAR measurements, *J South Am Earth Sci*, 72, 250–265, <https://doi.org/10.1016/j.jsames.2016.09.011>, 2016.](#)
- [Dionicio, V. and Sánchez, J. J.: Mapping of B-values, earthquake relocation, and coulomb stress changes during 1992-2007 in the murindó seismic zone, Colombia, *J Seismol*, 16, 375–387, <https://doi.org/10.1007/s10950-011-9263-6>, 2012.](#)
- 1975 [Dionicio, V., Pedraza-García, P. and Poveda, E. Datos de tensor de momento y mecanismo focal de sismos registrados por el Servicio Geológico Colombiano desde 2014 hasta 2021. *Boletín Geológico*, 50\(2\), in press, <https://doi.org/10.32685/0120-1425/bol.geol.50.2.2023.694>, 2023.](#)
- [Dziewonski, A. M., Chou, T. A., and Woodhouse, J. H.: Determination of earthquake source parameters from waveform data for studies of global and regional seismicity., *J Geophys Res*, 86, 2825–2852, <https://doi.org/10.1029/JB086iB04p02825>, 1981.](#)
- 1980 [Efron, B.: Bootstrap methods: another look at the jackknife. *Ann Stat*, 7, 1–26, 1979.](#)
- [Ehlers, T. A.: Crustal thermal processes and the interpretation of thermochronometer data, *Rev Mineral Geochem*, 58, 315–350, <https://doi.org/10.2138/rmg.2005.58.12>, 2005.](#)
- 1985 [Ekström, G., Nettles, M., and Dziewoński, A. M.: The global CMT project 2004-2010: Centroid-moment tensors for 13,017 earthquakes, *Physics of the Earth and Planetary Interiors*, 200–201, 1–9, <https://doi.org/10.1016/j.pepi.2012.04.002>, 2012.](#)
- [Engdahl, E. R., Di Giacomo, D., Sakarya, B., Gkarlaoui, C. G., Harris, J., and Storchak, D. A.: ISC-EHB 1964–2016, an Improved Data Set for Studies of Earth Structure and Global Seismicity, *Earth and Space Science*, 7, <https://doi.org/10.1029/2019EA000897>, 2020.](#)
- 1990

Ferry, N., Parent, L., Garric, G., Barnier, B., and Jourdain, N. C.: Mercator global Eddy permitting ocean reanalysis GLORYS1V1: Description and results, *Mercator-Ocean Quarterly Newsletter*, 34, 15–27, 2010.

1995 Gentili, S., Sugan, M., Peruzza, L., and Schorlemmer, D.: Probabilistic completeness assessment of the past 30 years of seismic monitoring in northeastern Italy, *Physics of the Earth and Planetary Interiors*, 186, 81–96, <https://doi.org/10.1016/j.pepi.2011.03.005>, 2011.

Gholamrezaie, E., Scheck-Wenderoth, M., Sippel, J., and Strecker, M. R.: Variability of the geothermal gradient across two differently aged magma-rich continental rifted margins of the Atlantic Ocean: The Southwest African and the Norwegian margins, *Solid Earth*, 9, 139–158, <https://doi.org/10.5194/se-9-139-2018>, 2018.

2000 Di Giacomo, D. and Storchak, D. A.: A scheme to set preferred magnitudes in the ISC Bulletin, *J Seismol*, 20, 555–567, <https://doi.org/10.1007/s10950-015-9543-7>, 2016.

Di Giacomo, D., Bondár, I., Storchak, D. A., Engdahl, E. R., Bormann, P., and Harris, J.: ISC-GEM: Global Instrumental Earthquake Catalogue (1900-2009), III. Re-computed MS and mb, proxy MW, final magnitude composition and completeness assessment, *Physics of the Earth and Planetary Interiors*, 239, 33–47, <https://doi.org/10.1016/j.pepi.2014.06.005>, 2015.

2005 Di Giacomo, D., Harris, J., and Storchak, D. A.: Complementing regional moment magnitudes to GCMT: A perspective from the rebuilt International Seismological Centre Bulletin, *Earth Syst Sci Data*, 13, 1957–1985, <https://doi.org/10.5194/essd-13-1957-2021>, 2021.

Goes, S., Govers, R., and Vacher, P.: Shallow mantle temperatures under Europe from P and S wave tomography, *Journal Of Geophysical Research-Solid Earth*, 105, 11153–11169, <https://doi.org/10.1029/1999jb900300>, 2000.

2010 Gómez-García, Á. M., Le Breton, E., Scheck-Wenderoth, M., Monsalve, G., and Anikiev, D.: 3D lithospheric structure of the Caribbean and north South American Plates and Rotation Files of Kinematic Reconstructions back to 90 Ma of the Caribbean Large Igneous Plateau, <https://doi.org/https://doi.org/10.5880/GFZ.4.5.2020.003>, 2020.

2015

Gómez-García, Á. M., Le Breton, E., Scheck-Wenderoth, M., Monsalve, G., and Anikiev, D.: The preserved plume of the Caribbean Large Igneous Plateau revealed by 3D data-integrative models, *Solid Earth*, 12, 275–298, <https://doi.org/10.5194/se-12-275-2021>, 2021.

2020

Gómez-García, Á. M., González, Á., Cacace, M., Scheck-Wenderoth, M., and Monsalve, G.: Hypocentral temperatures, geothermal gradients, crustal seismogenic depths and 3D thermal model of the Southern Caribbean and NW South America. *GFZ Data Services*. (temporary link: <https://dataservices.gfz-potsdam.de/panmetaworks/review/92360098bcf5658b89ffed28d0fbcfb1ebd0f9204f07f5b007ee6961268dd679/>).
2023.

González, Á.: The Spanish National Earthquake Catalogue: Evolution, precision and completeness, *J Seismol*, 21, 435–471, <https://doi.org/10.1007/s10950-016-9610-8>, 2017.

Grose, C. J. and Afonso, J. C.: Comprehensive plate models for the thermal evolution of oceanic lithosphere, *Geochemistry, Geophysics, Geosystems*, 14, 3751–3778, <https://doi.org/10.1002/ggge.20232>, 2013.

2025

Gutscher, M. A., Klingelhoefer, F., Theunissen, T., Spakman, W., Berthet, T., Wang, T. K., and Lee, C. S.: Thermal modeling of the SW Ryukyu forearc (Taiwan): Implications for the seismogenic zone and the age of the subducting Philippine Sea Plate (Huatung Basin), *Tectonophysics*, 692, 131–142, <https://doi.org/10.1016/j.tecto.2016.03.029>, 2016.

2030

Hasterok, D., Gard, M., and Webb, J.: On the radiogenic heat production of metamorphic, igneous, and sedimentary rocks, *Geoscience Frontiers*, 9, 1777–1794, <https://doi.org/10.1016/j.gsf.2017.10.012>, 2018.

He, C., Yao, W., Wang, Z., and Zhou, Y.: Strength and stability of frictional sliding of gabbro gouge at elevated temperatures, *Tectonophysics*, 427, 217–229, <https://doi.org/10.1016/j.tecto.2006.05.023>, 2007.

Hirth, G. and Beeler, N. M.: The role of fluid pressure on frictional behavior at the base of the seismogenic zone, *Geology*, 43, 223–226, <https://doi.org/10.1130/G36361.1>, 2015.

2035 [Hyndman, R. J. and Fan, Y.: Sample Quantiles in Statistical Packages, *American Statistician*, 50, 361–365, <https://doi.org/10.1080/00031305.1996.10473566>, 1996.](#)

[International Seismological Centre. ISC-EHB dataset, <https://doi.org/10.31905/PY08W6S3>, 2023a.](#)

[International Seismological Centre. On-line Bulletin, <https://doi.org/10.31905/D808B830>, 2023b.](#)

2040 [Jacquey, A., and Cacace, M.: GOLEM, a MOOSE-based application. *Zenodo*. <http://doi.org/10.5281/zenodo.999400>, 2017.](#)

[Kanamori, H.: The energy release in great earthquakes, 82, 2981–2987, 1977.](#)

[Kellogg, J. N., Camelio, G. B. F., and Mora-Páez, H.: Cenozoic tectonic evolution of the North Andes with constraints from volcanic ages, seismic reflection, and satellite geodesy, Elsevier Inc., 69–102 pp., <https://doi.org/10.1016/b978-0-12-816009-1.00006-x>, 2019.](#)

2045 [Kennan, L. and Pindell, J. L.: Dextral shear, terrane accretion and basin formation in the Northern Andes: best explained by interaction with a Pacific-derived Caribbean Plate?. *Geological Society, London, Special Publications*, 328, 487–531, <https://doi.org/10.1144/SP328.20>, 2009.](#)

[Kerr, A. C.: Oceanic Plateaus, in: *Treatise on Geochemistry: Second Edition*, vol. 4, Elsevier Ltd., Oxford, 631–667, <https://doi.org/10.1016/B978-0-08-095975-7.00320-X>, 2014.](#)

2050 [King, D. S. H. and Marone, C.: Frictional properties of olivine at high temperature with applications to the strength and dynamics of the oceanic lithosphere, *J Geophys Res Solid Earth*, 117, 1–16, <https://doi.org/10.1029/2012JB009511>, 2012.](#)

[Klitzke, P., Luzi-Helbing, M., Schicks, J. M., Cacace, M., Jacquey, A. B., Sippel, J., Scheck-Wenderoth, M., and Faleide, J. I.: Gas hydrate stability zone of the Barents Sea and Kara Sea region, *Energy Procedia*, 97, 302–309, <https://doi.org/10.1016/j.egypro.2016.10.005>, 2016.](#)

2055 [https://doi.org/10.1016/j.egypro.2016.10.005](#), 2016.

Liu, X., Currie, C. A., and Wagner, L. S.: Cooling of the continental plate during flat-slab subduction, *Geosphere*, 18, 49–68, <https://doi.org/10.1130/GES02402.1>, 2021.

Li, Y. and Toksoz, N.: Study of the source process of the 1992 Colombia Ms=7.3 earthquake with the empirical Green's function method, *Geophys Res Lett*, 20, 1087–1090, 1993.

2060 Lucazeau, F.: Analysis and mapping of an updated terrestrial heat flow data set. *Geochemistry, Geophysics, Geosystems*, 4001–4024, <https://doi.org/10.1029/2019gc008389>, 2019.

Marcaillou, B., Charvis, P., and Collot, J. Y.: Structure of the Malpelo Ridge (Colombia) from seismic and gravity modelling, *Marine Geophysical Research*, 27, 289–300, <https://doi.org/10.1007/s11001-006-9009-y>, 2006.

2065 Marone, C. and Saffer, D. M.: The Mechanics of Frictional Healing and Slip Instability During the Seismic Cycle. Elsevier B.V., 111–138 pp., <https://doi.org/10.1016/B978-0-444-53802-4.00092-0>, 2015.

Marone, C. and Scholz, C. H.: The depth of seismic faulting and the upper transition from stable to unstable slip regimes, *Geophys Res Lett*, 15, 621–624, <https://doi.org/10.1029/GL015i006p00621>, 1988.

McKenzie, D., Jackson, J., and Priestley, K.: Thermal structure of oceanic and continental lithosphere, *Earth Planet Sci Lett*, 233, 337–349, <https://doi.org/10.1016/j.epsl.2005.02.005>, 2005.

2070 Meeßen, C.: VelocityConversion, <https://doi.org/http://doi.org/10.5880/GFZ.6.1.2017.001>, 2017.

Mitchell, E. K., Fialko, Y., and Brown, K. M.: Frictional properties of gabbro at conditions corresponding to slow slip events in subduction zones, *Geochemistry, Geophysics, Geosystems*, 16, 4006–4020, <https://doi.org/10.1002/2015GC006093>, 2015.

2075 Molchan, G. M.: Strategies in strong earthquake prediction, *Physics of the Earth and Planetary Interiors*, 61, 84–98, [https://doi.org/10.1016/0031-9201\(90\)90097-H](https://doi.org/10.1016/0031-9201(90)90097-H), 1990.

Molchan, G. M.: Structure of optimal strategies in earthquake prediction, *Tectonophysics*, 193, 267–276, [https://doi.org/10.1016/0040-1951\(91\)90336-Q](https://doi.org/10.1016/0040-1951(91)90336-Q), 1991.

Molchan, G. M. and Kagan, Y. Y.: Earthquake prediction and its optimization, *J Geophys Res.*, 97, 4823–4838, <https://doi.org/10.1029/91JB03095>, 1992.

2080 Montes, C., Rodríguez-Corcho, A. F., Bayona, G., Hoyos, N., Zapata, S., and Cardona, A.: Continental margin response to multiple arc-continent collisions: The northern Andes-Caribbean margin, *Earth Sci Rev.* 198, 102903, <https://doi.org/10.1016/j.earscirev.2019.102903>, 2019.

Mora-Bohórquez, J. A., Oncken, O., Le Breton, E., Mejía-Ibañez, M., Veloza, G., Mora, A., Vélez, V., and De Freitas, M.: Formation and Evolution of the Lower Magdalena Valley Basin and San Jacinto Fold Belt of Northwestern Colombia: Insights from Upper Cretaceous to Recent Tectono-Stratigraphy, in: *The Geology of Colombia, Volume 3 Paleogene – Neogene*. Servicio Geológico Colombiano, Publicaciones Geológicas Especiales., vol. 3, edited by: Gómez, J. and Mateus-Zabala, D., 21–66, <https://doi.org/10.32685/pub.esp.37.2019.02.21>, 2020.

2085 Mosquera-Machado, S., Lalinde-Pulido, C., Salcedo-Hurtado, E., and Michetti, A. M.: Ground effects of the 18 October 1992, Murindo earthquake (NW Colombia), using the Environmental Seismic Intensity Scale (ESI 2007) for the assessment of intensity, *Geol Soc Spec Publ.* 316, 123–144, <https://doi.org/10.1144/SP316.7>, 2009.

Neill, I., Kerr, A. C., Hastie, A. R., Stanek, K.-P., and Millar, I. L.: Origin of the Aves Ridge and Dutch-Venezuelan Antilles: interaction of the Cretaceous “Great Arc” and Caribbean-Colombian Oceanic Plateau?, *J Geol Soc London*, 168, 333–348, <https://doi.org/10.1144/0016-76492010-067>, 2011.

2095 Noriega-Londoño, S., Restrepo-Moreno, S. A., Vinasco, C., Bermúdez, M. A., and Min, K.: Thermochronologic and geomorphometric constraints on the Cenozoic landscape evolution of the Northern Andes: Northwestern Central Cordillera, Colombia, *Geomorphology*, 351, <https://doi.org/10.1016/j.geomorph.2019.106890>, 2020.

Oleskevich, D., Hyndman, R., and Wang, K.: The updip and downdip limits to great subduction earthquakes: Thermal and structural models of Cascadia, south Alaska, SW Japan, and Chile, *J Geophys Res*, 104, 14965–14991, 1999.

2100 Omuralieva, A. M., Hasegawa, A., Matsuzawa, T., Nakajima, J., and Okada, T.: Lateral variation of the cutoff depth of shallow earthquakes beneath the Japan Islands and its implications for seismogenesis, *Tectonophysics*, 518–521, 93–105, <https://doi.org/10.1016/j.tecto.2011.11.013>, 2012.

Pagani, M., García-Pelaez, J., Gee, R., Johnson, K., Poogi, R., Styron, G., Weatherill, M., Simionato, D., Viganò, D., Danciu, L., and Monelli, D.: Global Earthquake Model (GEM) Seismic Hazard Map (version 2018.1 - December 2018), <https://doi.org/10.13117/GEM-GLOBAL-SEISMIC-HAZARD-MAP-2018.1>, 2018.

2105 Paris, G., Machette, M. N., Dart, R. L., and Haller, K. M.: Map and database of Quaternary faults and folds in Colombia and its offshore regions, 61 pp., 2000.

Pavlis, N. K., Holmes, S. A., Kenyon, S. C., and Factor, J. K.: The development and evaluation of the Earth Gravitational Model 2008 (EGM2008), *J Geophys Res Solid Earth*, 117, 1–38, <https://doi.org/10.1029/2011JB008916>, 2012.

2110 Pousse-Beltran, L., Vassallo, R., Audemard, F., Jouanne, F., Oropeza, J., Garambois, S., and Aray, J.: Earthquake geology of the last millennium along the Boconó Fault, Venezuela, *Tectonophysics*, 747–748, 40–53, <https://doi.org/10.1016/j.tecto.2018.09.010>, 2018.

Poveda, E., Monsalve, G., and Vargas, C.: Receiver functions and crustal structure of the northwestern Andean region, Colombia, *J Geophys Res Solid Earth*, 2408–2425, <https://doi.org/10.1002/2014JB011304>, 2015.

2115 Poveda, E., Julià, J., Schimmel, M., and Perez-Garcia, N.: Upper and Middle Crustal Velocity Structure of the Colombian Andes From Ambient Noise Tomography: Investigating Subduction-Related Magmatism in the Overriding Plate, *J Geophys Res Solid Earth*, 123, 1459–1485, <https://doi.org/10.1002/2017JB014688>, 2018.

2120 [Quintero, R., Zahradnk, J., Güendel, F., Campos-Durán, D., Alvarado, G. E., and Boutet, J. T.: Subduction transition and relation to upper plate faults revealed by the 2019 Mw 6.0 and 6.2 Costa Rica-Panama border earthquakes. *Tectonophysics*, 851, <https://doi.org/10.1016/j.tecto.2023.229759>, 2023.](#)

[Reguzzoni, M. and Sampietro, D.: GEMMA: An Earth crustal model based on GOCE satellite data. *International Journal of Applied Earth Observation and Geoinformation*, 35, 31–43, <https://doi.org/10.1016/j.jag.2014.04.002>, 2015.](#)

2125 [Restrepo, J. J. and Toussaint, J. F.: Terranes and continental accretion in the Colombian Andes. *Episodes*, 11, 189–193, <https://doi.org/10.18814/epiugs/1988/v11i3/006>, 1988.](#)

[Rodríguez Picada, C., Scheck-Wenderoth, M., Cacace, M., Bott, J., and Strecker, M. R.: Long-Term Lithospheric Strength and Upper-Plate Seismicity in the Southern Central Andes, 29°–39°S. *Geochemistry Geophysics Geosystems*, 23, <https://doi.org/10.1029/2021GC010171>, 2022.](#)

2130 [Salazar, W., Brown, L., Hernández, W., and Guerra, J.: An Earthquake Catalogue for El Salvador and Neighboring Central American Countries \(1528-2009\) and Its Implication in the Seismic Hazard Assessment. *Journal of Civil Engineering and Architecture*, 7, 1018–1045, <https://doi.org/10.17265/1934-7359/2013.08.011>, 2013.](#)

[Servicio Geológico Colombiano. Catálogo Mecanismo Focal y Tensor Momento. \[http://bdrsnc.sgc.gov.co/sismologia1/sismologia/focal_seiscomp_3/index.html\]\(http://bdrsnc.sgc.gov.co/sismologia1/sismologia/focal_seiscomp_3/index.html\), 2023.](#)

2135 [Schaeffer, A. J. and Lebedev, S.: Global shear speed structure of the upper mantle and transition zone. *Geophys J Int*, 194, 417–449, <https://doi.org/10.1093/gji/ggt095>, 2013.](#)

[Scheck-Wenderoth, M. and Maystrenko, Y. P.: Deep control on shallow heat in sedimentary basins. *Energy Procedia*, 40, 266–275, <https://doi.org/10.1016/j.egypro.2013.08.031>, 2013.](#)

[Schellart, W. P. and Strak, V.: Geodynamic models of short-lived, long-lived and periodic flat slab subduction. *Geophys J Int*, 226, 1517–1541, <https://doi.org/10.1093/gji/ggab126>, 2021.](#)

- 2140 [Scholz, C. H.: The Mechanics of Earthquakes and Faulting, 3rd Edition., Cambridge University Press, 471 pp., 2019.](#)
- [Schorlemmer, D., Mele, F., and Marzocchi, W.: A completeness analysis of the National Seismic Network of Italy, *J Geophys Res*, 115, 1–12, <https://doi.org/10.1029/2008jb006097>, 2010.](#)
- [Sibson, R.: Fault zone models, heat flow, and the depth distribution of earthquakes in the continental crust of the United States, *Bull. Seismol. Soc. Am.*, 72, 151–163, 1982.](#)
- 2145 [Sokos, E. N. and Zahradnik, J.: ISOLA a Fortran code and a Matlab GUI to perform multiple-point source inversion of seismic data, *Comput Geosci*, 34, 967–977, <https://doi.org/10.1016/j.cageo.2007.07.005>, 2008.](#)
- [Storchak, D. A., Harris, J., Brown, L., Lieser, K., Shumba, B., and Di Giacomo, D.: Rebuild of the Bulletin of the International Seismological Centre \(ISC\)—part 2: 1980–2010, *Geosci Lett*, 7, <https://doi.org/10.1186/s40562-020-00164-6>, 2020.](#)
- 2150 [Styron, R., García-Pelaez, J., and Pagani, M.: CCAF-DB: The Caribbean and Central American active fault database, *Natural Hazards and Earth System Sciences*, 20, 831–857, <https://doi.org/10.5194/nhess-20-831-2020>, 2020.](#)
- [Sun, M., Bezada, M. J., Cornthwaite, J., Prieto, G. A., Niu, F., and Levander, A.: Overlapping slabs: Untangling subduction in NW South America through finite-frequency teleseismic tomography, *Earth Planet Sci Lett*, 577, 117253, <https://doi.org/10.1016/j.epsl.2021.117253>, 2022.](#)
- 2155 [Tanaka, A.: Geothermal gradient and heat flow data in and around Japan \(II\): Crustal thermal structure and its relationship to seismogenic layer, *Earth, Planets and Space*, 56, 1195–1199, <https://doi.org/10.1186/BF03353340>, 2004.](#)
- [Tse, S. T. and Rice, J. R.: Crustal earthquake instability in relation to the depth variation of frictional slip properties, *J Geophys Res*, 91, 9452, <https://doi.org/10.1029/jb091ib09p09452>, 1986.](#)

2160 [Turcotte, D. L. and Schubert, G.: Geodynamics, 3rd ed., Cambridge: Cambridge University Press, 623 pp., https://doi.org/10.1017/CBO9780511843877, 2014.](#)

[Ueda, T., Obata, M., Ozawa, K., and Shimizu, I.: The Ductile-to-Brittle Transition Recorded in the Balmuccia Peridotite Body, Italy: Ambient Temperature for the Onset of Seismic Rupture in Mantle Rocks, *J Geophys Res Solid Earth*, 125, https://doi.org/10.1029/2019JB017385, 2020.](#)

2165 [Veloza, G., Styron, R., and Taylor, M.: Open-source archive of active faults for northwest South America, *GSA Today*, 22, 4–10, https://doi.org/10.1130/GSAT-G156A.1, 2012.](#)

[Vilà, M., Fernández, M., and Jiménez-Munt, I.: Radiogenic heat production variability of some common lithological groups and its significance to lithospheric thermal modeling, *Tectonophysics*, 490, 152–164, https://doi.org/10.1016/j.tecto.2010.05.003, 2010.](#)

2170 [Wagner, L. S., Jaramillo, J. S., Ramírez-Hoyos, L. F., Monsalve, G., Cardona, A., and Becker, T. W.: Transient slab flattening beneath Colombia, *Geophys Res Lett*, 44, 6616–6623, https://doi.org/10.1002/2017GL073981, 2017.](#)

[Weatherall, P., Marks, K. M., Jakobsson, M., Schmitt, T., Tani, S., Arndt, J. E., Rovere, M., Chayes, D., Ferrini, V., and Wigley, R.: A new digital bathymetric model of the world's oceans, *Earth and Space Science*, 2, 331–345, https://doi.org/10.1002/2015EA000107, 2015.](#)

2175 [Weston, J., Engdahl, E. R., Harris, J., Di Giacomo, D., and Storchak, D. A.: ISC-EHB: Reconstruction of a robust earthquake data set, *Geophys J Int*, 214, 474–484, https://doi.org/10.1093/gji/ggy155, 2018.](#)

[Wiemer, S. and Wyss, M.: Mapping the frequency-magnitude distribution in asperities: An improved technique to calculate recurrence times?, *J Geophys Res Solid Earth*, 102, 15115–15128, https://doi.org/10.1029/97jb00726, 1997.](#)

2180 [Wiemer, S. and Wyss, M.: Minimum magnitude of completeness in earthquake catalogs: Examples from Alaska, the Western United States, and Japan, *Bulletin of the Seismological Society of America*, 90, 859–869, https://doi.org/10.1785/0119990114, 2000.](#)

Wimpenny, S.: Weak, Seismogenic Faults Inherited From Mesozoic Rifts Control Mountain Building in the Andean Foreland, *Geochemistry, Geophysics, Geosystems*, 23, 1–19, <https://doi.org/10.1029/2021GC010270>, 2022.

Wimpenny, S. and Watson, C. S.: gWFM: A global catalog of moderate-magnitude earthquakes studied using teleseismic body waves, *Seismological Research Letters*, 92, 212–226, <https://doi.org/10.1785/0220200218>, 2020.

Wimpenny, S., Copley, A., Benavente, C., and Aguirre, E.: Extension and Dynamics of the Andes Inferred From the 2016 Parina (Huarichancara) Earthquake, *J Geophys Res Solid Earth*, 123, 8198–8228, <https://doi.org/10.1029/2018JB015588>, 2018.

Woessner, J. and Wiemer, S.: Assessing the quality of earthquake catalogues: Estimating the magnitude of completeness and its uncertainty, *Bulletin of the Seismological Society of America*, 95, 684–698, <https://doi.org/10.1785/0120040007>, 2005.

Wu, W. N., Yen, Y. T., Hsu, Y. J., Wu, Y. M., Lin, J. Y., and Hsu, S. K.: Spatial variation of seismogenic depths of crustal earthquakes in the Taiwan region: Implications for seismic hazard assessment, *Tectonophysics*, 708, 81–95, <https://doi.org/10.1016/j.tecto.2017.04.028>, 2017.

Zechar, J. D. and Jordan, T. H.: Testing alarm-based earthquake predictions, *Geophys J Int*, 172, 715–724, <https://doi.org/10.1111/j.1365-246X.2007.03676.x>, 2008.

Zielke, O., Schorlemmer, D., Jónsson, S., and Mai, P. M.: Magnitude-dependent transient increase of seismogenic depth, *Seismological Research Letters*, 91, 2182–2191, <https://doi.org/10.1785/0220190392>, 2020.

Zuza, A. V. and Cao, W.: Seismogenic thickness of California: Implications for thermal structure and seismic hazard, *Tectonophysics*, 782–783, 228426, <https://doi.org/10.1016/j.tecto.2020.228426>, 2020.

Eliminado: Acosta, J., Velandia, F., Osorio, J., Lonergan, L. and Mora, H.: Strike-slip deformation within the Colombian Andes, *Geol. Soc. Spec. Publ.*, 272(January), 303–319, doi:10.1144/GSL.SP.2007.272.01.16, 2007.¶
ANH: Banco de información petrolera, [online] Available from: [https://www.anh.gov.co/Banco de informacion petrolera/EPIS/Paginas/default.aspx](https://www.anh.gov.co/Banco%20de%20informacion%20petrolera/EPIS/Paginas/default.aspx) (Accessed 21 March 2020), 2020.¶
Arcila, M., García, J., Montejo, J., Eraso, J., Valcarcel, J., Mora, M., Viganò, D., Pagani, M. and Díaz, F.: Modelo nacional de amenaza sísmica para Colombia, 2020.¶
Arvidsson, R., Boutet, J. T. and Kulhanek, O.: Foreshocks and aftershocks of the Mw=7.1, 1992, earthquake in the Atrato region, Colombia, *J. Seismol.*, 6, 1–11, 2002.¶
Audemard, F. A. M.: Paleoseismicity studies on the Oca-Ancón fault system, northwestern Venezuela, *Tectonophysics*, 259(1–3), 67–80, doi:10.1016/0040-1951(95)00144-1, 1996.¶
Avellaneda-Jiménez, D. S., Monsalve, G., León, S. and Gómez-García, A. M.: Insights into Moho depth beneath the northwestern Andean region from gravity data inversion, *Geophys. J. Int.*, 229(3), 1964–1977, doi:10.1093/gji/ggac041, 2022.¶
Becker, T. W., Lowry, A. R., Faccenna, C., Schmandt, B., Borsa, A. and Yu, C.: Western US intermountain seismicity caused by changes in upper mantle flow, *Nature*, 524(7566), 458–461, doi:10.1038/nature14867, 2015.¶
Biegalski, K. F., Bohlin, J., Carter, J. A., Coyne, J., Dompierre, D., Novosel, G. and Rinehart, C.: Formats and protocols for messages – IMS1.0. International Data Center & Science Applications International Corporation. Document SAIC-99/3004., 1999.¶
Bondár, I. and Storchak, D.: Improved location procedures at the International Seismological Centre, *Geophys. J. Int.*, 186(3), 1220–1244, doi:10.1111/j.1365-246X.2011.05107.x, 2011.¶
Bormann, P.: Are new data suggesting a revision of the current Mw and Me scaling formulas?, *J. Seismol.*, 19(4), 989–1002, doi:10.1007/s10950-015-9507-y, 2015.¶
Cacace, M. and Jacquey, A. B.: Flexible parallel implicit modelling of coupled thermal-hydraulic-mechanical processes in fractured rocks, *Solid Earth*, 8(5), 921–941, doi:10.5194/se-8-921-2017, 2017.¶
Cacace, M. and Scheck-Wenderoth, M.: Why intracratonic basins subside longer: 3-D feedback effects of lithospheric cooling and sedimentation on the flexural strength of the lithosphere, *J. Geophys. Res. Solid Earth*, 121, 3742–3761, doi:10.1002/2015JB012682, 2016.¶
Chen, W.-P. and Molnar, P.: Focal depths of intracratonic and intraplate earthquakes and their implications for the thermal and mechanical properties of the lithosphere., *J. Geophys. Res.*, 88(B5), 4183–4214, doi:10.1029/jb088ib05p04183, 1983.¶
Chen, W. P., Yu, C. Q., Tseng, T. L., Yang, Z., Wang, C. yuen, Ning, J. and Leonard, T.: Moho, seismogenesis, and rheology of the lithosphere, *Tectonophysics*, 609(January 2021), 491–503, doi:10.1016/j.tecto.2012.12.019, 2013.¶
Chiarrabba, C. and De Gori, P.: The seismogenic thickness in Italy: constraints on potential magnitude and seismic hazard, *Terra Nov.*, 28(6), 402–408, doi:10.1111/ter.12233, 2016.¶
Dionicio, V. and Sánchez, J. J.: Mapping of B-values, earthquake relocation, and coulomb stress changes during 1992–2007 in the murindó seismic zone, Colombia, *J. Seismol.*, 16(3), 375–387, doi:10.1007/s10950-011-9263-6, 2012.¶
Efron, B.: Bootstrap methods: another look at the jackknife, *Ann. Stat.*, 7(1), 1–26, 1979.¶
Ehlers, T. A.: Crustal thermal processes and the interpretation of thermochronometer data, *Rev. Mineral. Geochemistry*, 58, 315–350, doi:10.2138/rmg.2005.58.12, 2005.¶
Ferry, N., Parent, L., Garric, G., Barnier, B. and Jourdain, N. C.: ...

Con formato: Normal

Eliminado: 38¶